JGR Solid Earth

RESEARCH ARTICLE
10.1029/2023JB027149

Modeling and Quantifying Parameter Uncertainty of Co-Seismic Non-Classical Nonlinearity in Rocks

Zihua Niu[1], **Alice-Agnes Gabriel**[1,2], **Linus Seelinger**[3], **and Heiner Igel**[1]

[1]Department of Earth and Environmental Sciences, Ludwig-Maximilians-Universität München, Munich, Germany, [2]Scripps Institution of Oceanography, UC San Diego, La Jolla, CA, USA, [3]Institute for Applied Mathematics, Heidelberg University, Heidelberg, Germany

Key Points:

- We analyze two physical models suitable for simulations of nonlinear elastic wave propagation observed in the laboratory
- The experimentally observed co-seismic acoustic modulus drop can be explained with nonlinear damage models
- We use the Markov chain Monte Carlo method to explore connections and uncertainties of nonlinear parameters

Correspondence to:
Z. Niu,
zniu@geophysik.uni-muenchen.de

Citation:
Niu, Z., Gabriel, A.-A., Seelinger, L., & Igel, H. (2024). Modeling and quantifying parameter uncertainty of co-seismic non-classical nonlinearity in rocks. *Journal of Geophysical Research: Solid Earth*, *129*, e2023JB027149. https://doi.org/10.1029/2023JB027149

Received 2 JUN 2023
Accepted 10 DEC 2023

Author Contributions:
Conceptualization: Zihua Niu, Alice-Agnes Gabriel, Heiner Igel
Formal analysis: Zihua Niu, Alice-Agnes Gabriel, Linus Seelinger, Heiner Igel
Funding acquisition: Alice-Agnes Gabriel, Heiner Igel
Investigation: Zihua Niu
Methodology: Zihua Niu, Alice-Agnes Gabriel, Linus Seelinger, Heiner Igel
Project Administration: Alice-Agnes Gabriel, Heiner Igel
Resources: Alice-Agnes Gabriel, Heiner Igel
Software: Zihua Niu, Alice-Agnes Gabriel, Linus Seelinger
Supervision: Alice-Agnes Gabriel, Heiner Igel
Validation: Zihua Niu
Visualization: Zihua Niu, Alice-Agnes Gabriel

Abstract Dynamic perturbations reveal unconventional nonlinear behavior in rocks, as evidenced by field and laboratory studies. During the passage of seismic waves, rocks exhibit a decrease in elastic moduli, slowly recovering after. Yet, comprehensive physical models describing these moduli alterations remain sparse and insufficiently validated against observations. Here, we demonstrate the applicability of two physical damage models—the internal variable model (IVM) and the continuum damage model (CDM)—to provide quantitative descriptions of nonlinear co-seismic elastic wave propagation observations. While the IVM uses one internal variable to describe the evolution of elastic material moduli, the CDM damage variable is a mathematical representation of microscopic defects. We recast the IVM and CDM models as nonlinear hyperbolic partial differential equations and implement 1D and 2D numerical simulations using an arbitrary high-order discontinuous Galerkin method. We verify the modeling results with co-propagating acousto-elastic experimental measurements. Subsequently, we infer the parameters for these nonlinear models from laboratory experiments using probabilistic Bayesian inversion and 2D simulations. By adopting the Adaptive Metropolis Markov chain Monte Carlo method, we quantify the uncertainties of inferred parameters for both physical models, investigating their interplay in 70,000 simulations. We find that the damage variables can trade off with the stress-strain nonlinearity in discernible ways. We discuss physical interpretations of both damage models and that our CDM quantitatively captures an observed damage increase with perturbation frequency. Our results contribute to a more holistic understanding of co-seismic damage and post-seismic recovery after earthquakes bridging the worlds of theoretical analysis and laboratory findings.

Plain Language Summary Rocks react to earthquakes by softening when seismic waves—the energy released by earthquakes—pass through them. Observations of such rock softening during the passage of seismic waves are common both in the laboratory and in the field. Interestingly, rocks gradually harden again once the shaking stops. Different physical mechanisms have been proposed to explain the observations. In this study, we put two existing theories to the test. One assumes that a term in the internal energy of the material increases with damage accumulation, while the other incorporates the opening and closing of micro-cracks. We implement them into a powerful simulation program called ExaHyPE. This allows us to model how nonlinear waves move through rocks. When we compare the computer simulation outcomes with real laboratory tests, we find that both models match what we see in reality. Studying thousands of simulations with different model parameters, we find some intriguing insights. For instance, the initial state of strain and the tiny cracks that open and close within the rock may be key to understanding the hardening and softening process. We hope to use these physical models in future earthquake simulations, offering more accurate predictions of how our Earth's crust reacts to earthquakes.

1. Introduction

Materials with micro- and mesoscale heterogeneities, such as rocks and cementitious materials, have been widely observed to exhibit non-classical nonlinearity (Guyer & Johnson, 1999; Johnson & Sutin, 2005; Van Den Abeele et al., 2000). In classical nonlinearity, researchers formulate stress as a nonlinear function of strain (e.g., the second order stress-strain models of Hamiel et al. (2011) and Murnaghan (1937); the third order stress-strain models in Landau et al. (1986)). Classical nonlinearity can describe how the speeds of elastic waves depend on the stress state of the material (Pao & Gamer, 1985), as well as different stress-strain relationships between compression and extension. Recent examples are the "bi-linear" models suggested by Panteleev et al. (2021) and Pecorari and Solodov (2006). However, these do not account for either the different stress-strain relationships

Writing – original draft: Zihua Niu
Writing – review & editing: Zihua Niu, Alice-Agnes Gabriel, Linus Seelinger, Heiner Igel

during loading and unloading or the time-dependent mechanical behavior of materials like rocks (Van Den Abeele et al., 2000). In this work, we define non-classical nonlinearity as the behavior of rocks that cannot be explained by formulating stress as a nonlinear function of strain. One type of such non-classical nonlinearity can be characterized by hysteresis models (Mayergoyz, 1985; McCall & Guyer, 1996; Preisach, 1935). Hysteresis models describe stress as a function of not only the current strain state but the strain history as well. Aside from hysteresis, researchers noticed that, under continuous dynamic external loads, the mechanical responses of rocks may change over time. Experimental observations of such non-classical nonlinearity were first reported in Ten Cate and Shankland (1996) from Nonlinear Resonance Ultrasound Spectroscopy (NRUS) experiments. In their NRUS experiments, the sample's dynamic response to the excitation at the same frequency unexpectedly varies depending on whether it is measured during the upward or downward sweep across different frequencies. We refer to TenCate (2011) and references therein for a comprehensive summary of the NRUS observations of the non-hysteresis type of non-classical nonlinearity.

Details on how rock moduli change during dynamic perturbations were first reported by Renaud et al. (2012) who performed Dynamic Acousto-elastic Testing (DAET) experiments on Barea sandstone. Since then, DAET experiments have been developed and conducted on different types of rock samples (e.g., Jin et al., 2018; Rivière et al., 2013, 2015). Figure 1 shows a recent DAET measurement by Shokouhi et al. (2017) on Berea sandstone samples. We will refer to all three phases illustrated in Figures 1b and 1c as "slow dynamics" (following e.g., Johnson & Sutin, 2005; Manogharan et al., 2021; Rivière et al., 2015; Shokouhi et al., 2017).

Similar observations have also been reported from the field since the pioneering work of Brenguier et al. (2008) and Sens-Schönfelder and Wegler (2006). Gassenmeier et al. (2016) monitor the change of seismic velocity around the station PATCX from the Integrated Plate Boundary Observatory Chile Network (IPOC) IPOC (2006). During the occurrence of the M_W 7.7 Tocopilla earthquake in Chile on 14 November 2007, Gassenmeier et al. (2016) observe a drop and subsequent recovery of seismic velocity within a radius of ≈2.3 km surrounding a station that is about 100 km away from the fault using coda wave interferometry in the frequency range of 4–6 Hz. Similar co-seismic velocity drops are reported to occur not only during large earthquakes but also due to intermediate earthquakes with magnitudes between M_W 5 and M_W 7. Brenguier et al. (2014) map the co-seismic velocity drop in Japan after the 2011 Tohoku-Oki earthquake (see Figure 1d) using data from the high sensitivity seismograph network (Hi-net) in Japan (Takanami et al., 2003). While it is commonly assumed that transient fluid effects are key to the observed velocity drop (Brenguier et al., 2014; Illien et al., 2022), Manogharan et al. (2021, 2022) find that a velocity drop during dynamic perturbations of fractured fluid-saturated rocks is not more significant than that of fractured dry rocks.

Despite phenomenologically comparable observations, it is currently unclear how relevant the non-classical nonlinearity observed in laboratory experiments is to the observed co-seismic velocity drops in the field and if an overarching theoretical physical framework can be established. Furthermore, despite the relatively low velocity drops (usually smaller than 1%) using ambient noises and coda wave interferometry (e.g., Brenguier et al., 2014; Gassenmeier et al., 2016; Illien et al., 2022), more recent measurements based on auto-correlation of a single station (Lu & Ben-Zion, 2022) or the combination of surface and borehole stations (Qin et al., 2020; Wang et al., 2021) show that the velocity drop can be higher than 10%. Unifying laboratory and field observations is challenged by the vastly different scales and sparsity of high-resolution observations. What is needed is an appropriate physical model that can be employed at both scales.

At the field scale, a range of models have been proposed to explain or predict source and site effects of nonlinearity on earthquake nucleation, rupture dynamics, and ground motions. The Masing-Prager-Ishlinski-Iwan (MPII) model (Iwan, 1967) has been implemented to study local non-linear site effects due to soft sediments (Oral et al., 2019, 2022; Roten et al., 2013, 2018). The MPII model reproduces the hysteretic stress-strain relations and can be extended to explain the excess pore pressure in liquefiable soils (Oral et al., 2019). The nonlinearity of fault zone deformation has been modeled as co-seismic off-fault brittle continuum damage (e.g., Thomas & Bhat, 2018; Xu et al., 2015), non-associative Drucker-Prager off-fault plasticity (e.g., Andrews, 2005; Wollherr et al., 2018), or explicit secondary tensile and shear fracturing (Gabriel et al., 2021; Okubo et al., 2020; Yamashita, 2000), using a volumetric representation of fault zones governed by reformulated rate-and-state friction laws (Pranger et al., 2022; Preuss et al., 2019, 2020) or phase-field inspired methods (e.g., Fei et al., 2023). However, a physical model that can be used to explain the co-seismic drop of wave speeds and subsequent recovery is currently missing. This paper focuses on identifying appropriate theoretical models that can be informed and verified by

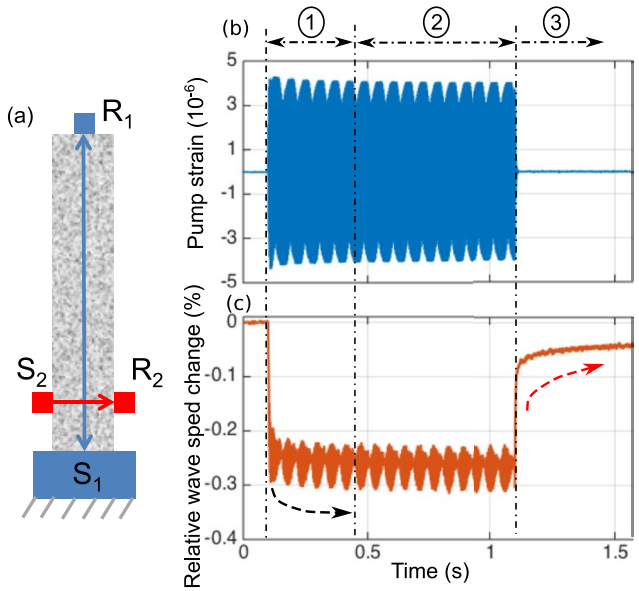

Figure 1. Dynamic acousto-elastic testing (DAET) by Shokouhi et al. (2017) on Berea sandstone samples. (a) The pump-probe system in DAET. S1-R1 is the pumping sensor pair. S1 is a piezoelectric ceramic disk glued to the sample. S1 generates a dynamic strain field (the pump field) with an amplitude of around 4×10^{-6} and a frequency of around 4.5 kHz. R1 is a miniature accelerometer that measures the dynamic strain field (the pump field) generated by S1. The probing ultrasonic transducer pair S2-R2 measures the change of the P-wave speed Δc_p due to the pump field. (b) The pump field, as measured with R1. (c) The measured relative change in P-wave speed $\Delta c_p / c_{p0}$, due to the pump field, with S2-R2. Here, c_{p0} is the initial P-wave speed of the sample. In response to the dynamic strain field from S1, the wave speed evolves in three consecutive phases: (1) As loading starts, the wave velocity of the sample reaches a non-equilibrium state and experiences an overall drop aside from fluctuations with the cyclic loading. This phase is referred to as the conditioning of the material and is marked by a dashed black curve with an arrow; (2) The overall drop of wave velocity stabilizes and reaches a new steady state; (3) After removing the cyclic loading, the velocity recovers over an extended period of time, illustrated by the dashed red curve with an arrow.

laboratory experiments and are applicable for future large-scale numerical simulations (e.g., Roten et al., 2023) of seismological observations on the field scale.

Over the past two decades, researchers have proposed different models to explain non-classical nonlinearity with physical processes at the microscopic scale. Delsanto and Scalerandi (2003) proposed a model that includes thermally activated random transitions between two different interstitial states. Since then, many studies have used the framework of adhesive contacts at rough crack surfaces to explain slow dynamics (Aleshin & Van Den Abeele, 2007; Lebedev & Ostrovsky, 2014; Pecorari, 2004; Wang et al., 2021). We briefly summarize the adhesive contact theory in Appendix E.

While the above physical models are firmly rooted in processes at the microscopic scale, they introduce a significant number of parameters. Many of these parameters are hard to constrain directly from observations. Also, the proposed models are restricted to 0D (oscillation) or 1D analysis. An extension to 2D and 3D would require a substantial effort, although it is crucial for the verification and interpretation of field observations. There also exist phenomenological models, with fewer parameters, that have been developed over the last two decades, such as the soft ratchet model of Vakhnenko et al. (2004, 2005). Their model includes a fast subsystem of displacement and a slow subsystem of ruptured intergrain cohesive bonds. The concentration of the ruptured bonds is represented by an internal (damage) variable that evolves to a stress-dependent equilibrium. Later, Favrie et al. (2015) fully couple these two subsystems.

Berjamin et al. (2017) extend the description of Favrie et al. (2015) by using one internal variable to describe the evolution of elastic material moduli. This model will be herein referred to as the internal variable model (IVM) in the following. IVM ensures that the kinematics of the internal variable complies with the laws of thermodynamics. The model can reproduce the conditioning and recovery phases of nonclassical nonlinear elasticity with only two additional parameters than those used in classical nonlinearity. However, their expression for the internal energy of the material contains a term that is not clearly linked to physical processes.

In this work, we offer a physics-based understanding of the origin of such a phenomenological term. To this end, we resort to continuum damage mechanics (CDM) (Kachanov, 1958, 1986). We show that the internal variable in Berjamin et al. (2017) is very similar to a scalar damage variable in typical CDM approaches (Chaboche, 1988). The scalar damage variable approach is popular in diffuse interface approaches, for example, to "smear out" sharp, discontinuous cracks via a smooth but rapid transition between intact and fully damaged material states (Borst et al., 2004; Tavelli et al., 2020). The Godunov–Peshkov–Romenski (GPR) model (Gabriel et al., 2021; Resnyansky et al., 2003; Romenski et al., 2007; Tavelli et al., 2020) uses the homogenization scheme based on the continuum mixture theory (Romenski & Toro, 2004) to define a material that is a mixture of a "totally-damaged" and an "undamaged" constituent. In other frameworks, the damage variable can be defined as the density of intergranular cavities or microcracks distributed within a solid. By assuming uniformly and omnidirectionally distributed cracks, Budiansky and O'Connell (1976) derive the elastic moduli as a function of the damage variable. Without assuming an omnidirectional distribution, Chaboche (1992), Desmorat (2016), and Lemaitre and Desmorat (2006) propose the "unilateral" damage model that can account for different elastic behaviors during extension and compression of the solid.

However, the above CDM-based damage models do not allow healing. The continuum damage healing model introduces an additional healing variable aside from the damage variable (Darabi et al., 2012; Oucif & Mauludin, 2018). A potentially simpler framework that can allow healing is the damage model proposed by Lyakhovsky, Ben-Zion, and Agnon (1997). It is based on homogenizing micro-cracks oriented perpendicular to

the maximum tension (or compression). This is different from other damage models based on the homogenization of cracks oriented uniformly and omnidirectionally (e.g., Borst et al., 2004; Budiansky & O'Connell, 1976; Chaboche, 1988). The internal energy of this model is not unconditionally decreasing with the increase of the damage variable. However, it has not yet been investigated how this model can be related to observed slow dynamics. We summarize these and other representative damage models with respect to non-classical nonlinearity in Table E1.

From the above overview of models, we notice that the models of Berjamin et al. (2017) and Lyakhovsky, Ben-Zion, and Agnon (1997) both have the potential to reproduce all three phases of slow dynamics with a small number of model parameters. In the following, we will focus on two models, IVM by Berjamin et al. (2017) and CDM by Lyakhovsky, Ben-Zion, and Agnon (1997), and will refer to them as "model B" and "model L," respectively, for brevity. We explore if they can quantitatively reproduce the modulus changes of rocks observed in laboratory experiments, as well as how well laboratory findings may constrain theoretical model parameters.

To investigate these questions, we implement both models in the arbitrary high-order discontinuous Galerkin (ADER-DG) solver ExaHyPE (Reinarz et al., 2020) and verify the numerical simulation results with experimental observations. We infer model parameters from laboratory measurements using a Markov chain Monte Carlo (MCMC, Metropolis et al., 1953) algorithm. This takes uncertainties due to measurement errors into account and allows us to investigate model parameters' relative importance and their interactions. Lastly, we discuss that the CDM model by Lyakhovsky, Ben-Zion, and Agnon (1997) may be a preferred model for large-scale wave propagation simulations capable of linking observations of co-seismic damage in the field with laboratory findings and CDM theory.

In Section 2, the two models of Berjamin et al. (2017) and Lyakhovsky, Ben-Zion, and Agnon (1997) (model L and model B hereafter) are summarized within the framework of thermodynamics. We propose a way to explain the origin of the phenomenological term in the model of Berjamin et al. (2017). We then describe the numerical simulation of the nonlinear wave propagation with the two models. This is followed by a description of the experiment that we will compare to the Bayesian problem used for parameter inference and the Adaptive Metropolis Markov chain Monte Carlo (AM-MCMC) method solving it. In Section 3, we compare the two models regarding the damage evolution during DAET and measured amplitude- and frequency-dependent damage. The inversion results of the model parameters are also shown. Finally, the performance and restrictions of the two models will be discussed in Section 4.

2. Method

We separate this section into two parts. We first detail the derivation of the nonlinear damage models based on the laws of thermodynamics. This approach ensures that the model parameterization we derive has a clear physical meaning. Based on our thermodynamically motivated derivation, we aim to infer physical constraints on slow dynamics that are beyond phenomenological descriptions. We then describe the experiment and the AM-MCMC method that we use to evaluate the model parameters.

2.1. The Thermodynamic Formulation of Nonlinear Damage Models

In the framework of CDM (see Chapter 3 of Zhang & Cai, 2010), a scalar variable can describe the changes in elastic moduli with damage. We start with the first law of thermodynamics,

$$\dot{e} = \dot{w} + \dot{q}, \tag{1}$$

where $\dot{(\cdot)}$ denotes the time derivative, e is the specific internal energy of the system normalized by volume, w is the external work per unit volume of the system and q is the absorbed heat from the environment per unit volume of the system. At the time scale of elastodynamic processes, the heat transfer and any possible heat sources are assumed to be negligible, that is, we assume an adiabatic process where $\dot{q} = 0$. In case of only considering mechanical work, the rate of external work is expressed as $\dot{w} = \underline{\underline{\sigma}} : \dot{\underline{\underline{\epsilon}}} = \sigma_{ij}\,\dot{\epsilon}_{ij}$ and $\underline{\underline{(\cdot)}}$ denotes a tensor of rank two.

The expression of the internal energy depends on the choice of state variables that are used to describe the system. For an elastic material, we chose the strain $\underline{\underline{\varepsilon}}$ and the specific entropy s as state variables. In addition, to incorporate the damage to the material, we include another scalar state variable α. This means $e \equiv e\left(s, \underline{\underline{\varepsilon}}, \alpha\right)$.

With the above definitions of state variables, the Gibbs identity can be written as

$$\dot{e} = T\dot{s} + \frac{\partial e}{\partial \underline{\underline{\varepsilon}}} : \dot{\underline{\underline{\varepsilon}}} + \frac{\partial e}{\partial \alpha}\dot{\alpha}, \tag{2}$$

where $T = \frac{\partial e}{\partial s} > 0$ is the absolute temperature.

Different nonlinear or damage models have different ways of defining the internal energy as a function of $\underline{\underline{\varepsilon}}$ and α. The combination of Equations 1 and 2, together with the earlier defined assumptions of $\dot{q} = 0$ and $\dot{w} = \underline{\underline{\sigma}} : \dot{\underline{\underline{\varepsilon}}}$, yields

$$T\dot{s} = \left(\underline{\underline{\sigma}} - \frac{\partial e}{\partial \underline{\underline{\varepsilon}}}\right) : \dot{\underline{\underline{\varepsilon}}} - \frac{\partial e}{\partial \alpha}\dot{\alpha}. \tag{3}$$

For a spontaneous process in an adiabatic system, $T\dot{s} = \left(\underline{\underline{\sigma}} - \frac{\partial e}{\partial \underline{\underline{\varepsilon}}}\right) : \dot{\underline{\underline{\varepsilon}}} - \frac{\partial e}{\partial \alpha}\dot{\alpha} \geq 0$, which is known as the Clausius–Duhem inequality (Truesdell, 1952). The inequality should hold for any given $\dot{\underline{\underline{\varepsilon}}}$ and $\dot{\alpha}$. If we further assume that $\underline{\underline{\sigma}}$ is independent of $\dot{\underline{\underline{\varepsilon}}}$, we derive

$$\underline{\underline{\sigma}} - \frac{\partial e}{\partial \underline{\underline{\varepsilon}}} = 0. \tag{4}$$

Otherwise, for any given value of $\frac{\partial e}{\partial \alpha}\dot{\alpha}$, we can always find a tensor $\dot{\underline{\underline{\varepsilon}}}$ that leads to a negative value of $T\dot{s}$. Substituting Equation 4 into the Clausius–Duhem inequality, we derive

$$\frac{\partial e}{\partial \alpha}\dot{\alpha} \leq 0, \tag{5}$$

where $\frac{\partial e}{\partial \alpha}$ can be any function of the state variables. Equation 5 describes the evolution of the damage variable α. A simple and non-trivial (non-zero) expression can be

$$\frac{\partial e}{\partial \alpha} = -\tau\dot{\alpha}, \tag{6}$$

where τ can be any non-negative constant or non-negative function of the state variables. In Equation 6, we see that damaged material will only heal $\left(\dot{\alpha} < 0\right)$ when $\tau > 0$ and $\frac{\partial e}{\partial \alpha} > 0$; otherwise damage will steadily accumulate. More specifically, our derivation indicates that the system's internal energy should at some point increase with an increase of damage, that is $\frac{\partial e}{\partial \alpha} > 0$, such that the healing of the material still obeys the second law of thermodynamics. Such interpretation is possible since we use the framework of a CDM. Substituting Equations 4 and 6 into Equation 3 yields the energy dissipation rate of the system.

$$\mathcal{D} = T\dot{s} = \begin{cases} 0 & \text{if } \tau = 0 \\ \frac{1}{\tau}\left(\frac{\partial e}{\partial \alpha}\right)^2 & \text{if } \tau > 0 \end{cases}. \tag{7}$$

Both model L (Lyakhovsky, Ben-Zion, & Agnon, 1997) and model B (Berjamin et al., 2017) describe the mechanisms of damage and recovery. But they are introduced under different assumptions regarding the form of the internal energy as a function of strain $\underline{\underline{\varepsilon}}$ and the damage variable α. The internal variable of Berjamin et al. (2017) is defined as

$$e = (1 - \alpha)\mathcal{E}\left(\underline{\underline{\varepsilon}}\right) + \phi(\alpha), \tag{8}$$

where $\phi(\alpha)$ is called the storage energy and increases with the development of damage. In the 1D case where only $\varepsilon_{xx} = \varepsilon$ is non-zero, Berjamin et al. (2017) express the elastic energy term in the internal energy as $\mathcal{E} = \left(\frac{1}{2} - \frac{\beta}{3}\varepsilon - \frac{\delta}{4}\varepsilon^2\right) M\varepsilon^2$ based on Landau's law (Landau et al., 1986), where $M = \lambda + 2\mu$ is acoustic modulus while λ and μ are the two Lamé parameters. In the 2D plane-strain case, Berjamin et al. (2019) use the Murnaghan's law $\mathcal{E} = \frac{\lambda+2\mu}{2} E_I^2 - 2\mu E_{II} + \frac{l+2m}{3} E_I^3 - 2mE_I E_{II} + nE_{III}$ (Murnaghan, 1937). l, m, and n are the three Murnaghan coefficients (third-order elastic constants), while $E_I = \epsilon_{kk}$, $E_{II} = 1/2\left((\epsilon_{kk})^2 - \epsilon_{ij}\epsilon_{ij}\right)$ and $E_{III} = \delta_{ijk}\epsilon_{i1}\epsilon_{j2}\epsilon_{k3}$ are three stress invariants that are defined in Berjamin et al. (2019). δ_{ijk} denotes Levi-Civita permutation symbol.

According to Equation 6, the damage evolution then reads

$$\dot{\alpha} = \frac{1}{\tau}\left(\mathcal{E}\left(\underline{\underline{\varepsilon}}\right) - \phi'(\alpha)\right), \tag{9}$$

where Berjamin et al. (2017) proposed two possible expressions of ϕ: $\phi'(\alpha) = \gamma_b \frac{\alpha}{1-\alpha^2}$ or $\phi'(\alpha) = \gamma_b \alpha$. The scaling factor τ is formulated as $\tau = \gamma_b \tau_b$, where γ_b is the scale of storage energy $\phi(\alpha)$ and τ_b is the time scale of damage evolution.

In the model L proposed by Lyakhovsky, Ben-Zion, and Agnon (1997) internal energy is defined as

$$e = \mathcal{E}\left(\underline{\underline{\varepsilon}}, \alpha\right) - \gamma I_1 \sqrt{I_2}, \tag{10}$$

where, in the linear elastic case, $\mathcal{E}\left(\underline{\underline{\varepsilon}}, \alpha\right) = \frac{\lambda}{2} I_1^2 + \mu I_2$, $I_1 = \varepsilon_{kk}$ and $I_2 = \varepsilon_{ij}\varepsilon_{ij}$ are the first and the second strain invariant, and γ is a third modulus that originates from the homogenization of parallel cracks (Lyakhovsky, Reches, et al., 1997). It is assumed that $\lambda = \lambda_0$, $\mu = \mu_0 - \alpha\mu_r$ and $\gamma = \alpha\gamma_r$. The corresponding damage kinematics is then derived by inserting Equation 10 into Equation 6

$$\begin{aligned} \dot{\alpha} &= C_d \gamma_r \left(I_1 \sqrt{I_2} - \xi_0 I_2\right) \\ &= C_d \gamma_r I_2 (\xi - \xi_0), \end{aligned} \tag{11}$$

where $\xi_0 = -\frac{\mu_r}{\lambda_r}$ and is a negative parameter for solid materials; $\xi = I_1/\sqrt{I_2}$ and C_d can be any non-negative function of the state variables $\underline{\underline{\epsilon}}$ and α. We note that the material heals $\left(\dot{\alpha} < 0\right)$ when $\xi - \xi_0 < 0$ and is damaged $\left(\dot{\alpha} > 0\right)$ when $\xi - \xi_0 > 0$.

A comparison of Equations 9 and 11 shows that both models in principle include the mechanism of healing. However, the crucial term ϕ for explaining slow dynamics in model B in Equation 8 has only limited physical meaning, which challenges the interpretation of the physical mechanisms driving the observed slow dynamics (Figure 1c). On the other hand, conditioning and healing were not yet explored using the model L of Lyakhovsky, Ben-Zion, and Agnon (1997).

So far we have summarized model L and model B in the same thermodynamics framework. Next, we explain why, based on model L, it may be physically plausible to include a term in the internal energy W that can increase with damage and how this term can result in both the conditioning during dynamic perturbations and the recovery after removing the perturbations. We here propose that the steady state (Phase 2 in Figure 1c) during perturbations can be recovered by assuming the following form of damage kinematics in Equation 12 for the model L that differentiates the evolution laws during the recovery from that during the damage. A recovery phase after dynamic perturbations can occur if an initial strain that satisfies $\xi - \xi_0 < 0$ exists. This strain level does not need to be large since ξ is only related to the relative magnitude of each strain component (i.e., the shape of the strain tensor).

$$\dot{\alpha} = \begin{cases} C_d(\alpha)\gamma_r I_2(\xi - \xi_0) & \text{if } \xi - \xi_0 > 0 \text{ and } \alpha \geq 0 \\ C_r(\alpha)\gamma_r I_2(\xi - \xi_0) & \text{if } \xi - \xi_0 \leq 0 \text{ and } \alpha \geq 0 \\ 0 & \text{if } \alpha < 0 \end{cases}. \tag{12}$$

The evolution laws during "damage" ($C_d(\alpha)$, the conditioning during dynamic perturbations) and "recovery" ($C_r(\alpha)$) are treated separately. The steady state (Phase 2 in Figure 1c) requires the increase of $C_d(\alpha)$, the decrease of

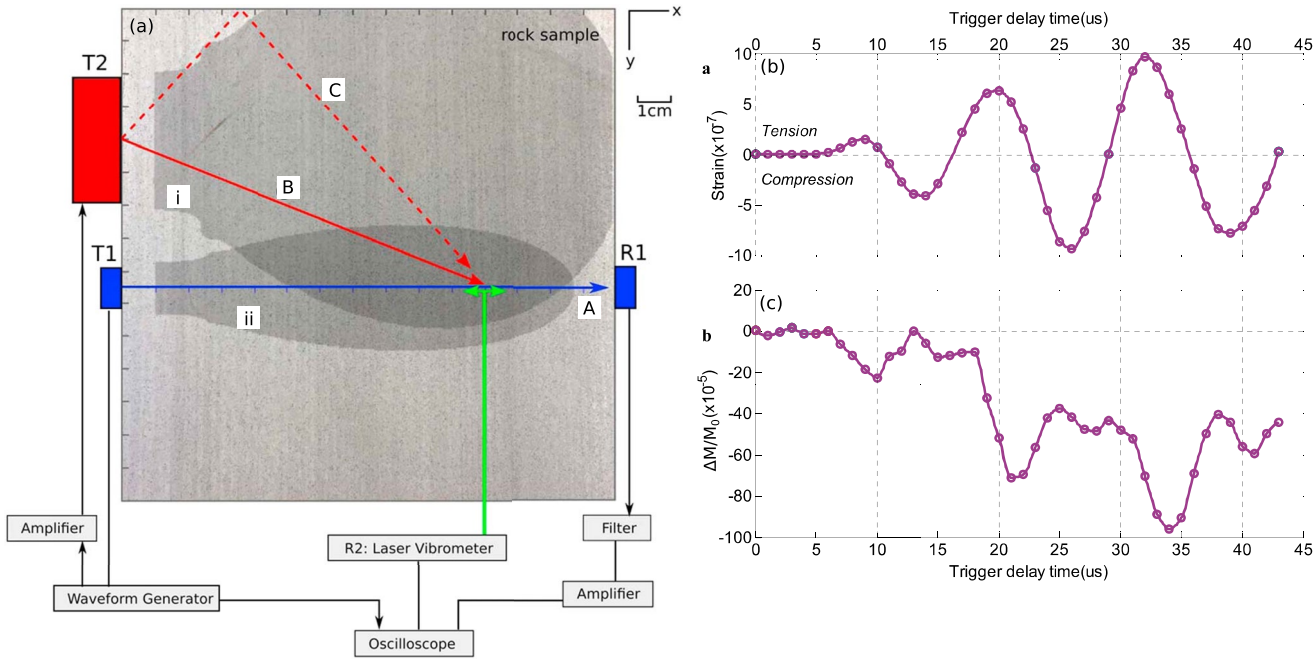

Figure 2. (a) Experimental setup to perform copropagating acousto-elastic testing (Figure adapted from Feng et al., 2018). T1 is a low-energy high-frequency transmission ultrasound (US) transducer, the probe, and R1 is the receiver of T1. T2 is a high-energy low frequency transmission US transducer. The induced velocity field is recorded by the laser vibrometer R2. The velocity field is converted to the strain field with the method described by Feng et al. (2018). The shadowed areas indicate the radiation pattern (amplitude as a function of angle) of (i) T2 and (ii) T1. Line A is the direct ray path from T1 to R1, line B is the direct ray path from T2 to a point of wave interaction at (8.5, 11.0) cm, and the dashed line C shows the ray path for the wave from T2 reflected at the top boundary of the sample that arrives at that same point of interaction at (8.5, 11.0) cm. (b) The strain (ε_{xx}) measured at the wavefront of the waves that are excited from T1 at different trigger time delays. Each data point is the averaged strain at the wavefront during its propagation from T1 to R1. (c) The estimated relative change in acoustic modulus, based on the travel time difference between T1 and R1, as a function of the trigger time delays. Acoustic modulus $M = \lambda + 2\mu$. M_0 is the M without the pumping signals, while ΔM is the change in M during the propagation of the pumping signals.

$C_r(\alpha)$ or both. At the same time, $C_d(\alpha)$ and $C_r(\alpha)$ are required to remain non-negative to preserve a non-decreasing entropy of the system according to Equation 7. With the above considerations, we choose $C_d(\alpha) = c_d \exp\left(-\frac{\alpha}{\alpha_d}\right)$ and $C_r(\alpha) = c_r\alpha$ to represent, respectively, the decrease of damage coefficient C_d and the increase of recovery coefficient C_r with the increase of the damage variable.

Our proposed damage evolution still follows the laws of thermodynamics. We show in Section 3 that the combination of Equation 12 and the existence of a well-defined initial strain level recovers many aspects of the observed slow dynamics.

2.2. Verification, Validation and Parameter Constraints Using Laboratory Observations

We implement both models in ExaHyPE (Reinarz et al., 2020), an engine built for solving nonlinear hyperbolic partial differential equations (PDEs) with the arbitrary high-order derivative discontinuous Galerkin (ADER-DG) method. In Appendix B, we verify the implementation by comparing our numerical solutions with those given by Berjamin et al. (2019), who implemented model B in 2D under plain-strain conditions using the finite volume method with flux limiters. We provide the comparison of our simulations with those from Berjamin et al. (2019) in Figure B1. In the following, we focus on validating the performance of model B and model L against laboratory observations.

We generate ensembles of our numerical simulations using the two models and compare them to laboratory measurements. One of the main advantages of model B (IVM) and model L (CDM) is that they have fewer parameters and, therefore, may be easier to constrain than models that are established on detailed physical processes at microscopic scales. We apply Bayesian inversion to quantify how well the model parameters can be constrained from laboratory experiments. Most laboratory experiments of slow dynamics are based on 1D setups. Feng et al. (2018) proposed an experimental setup (copropagating acousto-elastic testing, Figure 2) that enables the

observation of acoustic modulus change during the propagation of waves in a rock sample. In the following, we first describe the experimental setup. Next, we formulate a Bayesian inversion problem that we apply for quantitative characterization of the theoretical model parameters and their associated uncertainties with respect to reproducing laboratory results. The Bayesian inversion problem is solved with a MCMC (Metropolis et al., 1953) type method.

2.2.1. Laboratory Verification Experiment Measuring Slow Dynamics in 2D

The experiment is conducted using a sample of Crab Orchard sandstone of size 15 × 15 × 5 cm. Feng et al. (2018) attached two US transducers and one receiver to the rock sample as shown in Figure 2a. T1 is a low-energy high-frequency (HF) transmission US transducer, the probe, and R1 is an HF reception US transducer. T2 is a high-energy low frequency transmission US transducer, the pump, and R2 is the laser vibrometer. In the experiment, T2 generates a pumping signal with a frequency of 74 kHz. The particle velocity field excited by T2 is measured with the vibrometer R2 and the particle velocity is converted to the strain (ε_{xx}) along the ray path A between T1 and R1. The P-wave speed along the ray path A is probed with a 620 kHz signal from T1. The amplitude of the perturbation by T1 is of much lower amplitude than that by T2 and is therefore assumed to not perturb the strain field. Once T2 is triggered at t_0, T1 will send signals every 1 μs to measure the P-wave speed along the ray path A. The time difference between the signal from T1 and t_0 is called "trigger delay." The strain field at the wavefront of each trigger delay along the ray path A is averaged and shown in Figure 2b. The acoustic modulus change $\Delta M/M_0$ is computed from the change in P-wave speed of each trigger delay in Figure 2c.

Feng et al. (2018) explain the relation between the strain field and the acoustic modulus change with the nonlinear visco-elastic relationship. They observe a time shift of around 2 μs between the peak in the acoustic modulus change and in strain, which is fit by imposing a "delay time" Δt in the visco-elastic relationship. We show in this work that the data may also be explained with the proposed damage models without having to impose a "delay time" for explaining the time shift.

2.2.2. Probabilistic Inversion and Uncertainty Quantification With a Markov Chain Monte Carlo Approach

We begin by defining configurations of our two competing deterministic models, matching the experimental setup. Next, we augment the deterministic models by embedding them in a Bayesian inversion problem. This allows us to infer model parameters from data and discover their interactions, considering possible ambiguities and the effect of uncertainties in experimental measurements.

2.2.2.1. Deterministic Forward Models

We model the 2D slow dynamics experimental setup with both the L and the B models. The perturbation from T2 is simulated as a Dirichlet boundary condition distributed in the area where T2 is in contact with the sample. The remaining boundaries are treated as free surfaces with zero traction. As in the experiment, the strain ε_{xx} and the acoustic modulus change are averaged over the path of the wavefront between T1 and R1 for each trigger delay (every 1 μs between 0 and 39 μs).

In Equation 8 of model B, the first order nonlinearity in 2D Murnaghan's law already involves three parameters (l, m and n). The laboratory data are not sufficient to constrain all three parameters. Similar to the simplification made in the original paper of Feng et al. (2018), the change in $M = \lambda + 2\mu$, which is related to the speed of the P-wave, is simplified as a function of the damage parameters computed from the 2D simulation and the 1D first and second order nonlinearity parameters as in Equation 13.

$$M = M_0(1-\alpha)\left(1 - \beta\varepsilon_{xx} - \delta\varepsilon_{xx}^2\right), \tag{13}$$

where M_0 is the initial acoustic modulus of the undamaged rock sample before the perturbations. Such a relationship is also used by Berjamin et al. (2017) in the 1D formulation of their model. For model L, we derive the variations in the speed of the P-wave with the strain tensor and the damage parameter in Appendix A.

In model B, the two parameters that control the damage evolution are γ_b and τ_b in Equation 9. Combining these with the two nonlinear parameters in Equation 13, the parameters to be inverted are β, δ, γ_b, and τ_b.

In model L, it is

$$\dot{\alpha} = \begin{cases} c_d \gamma_r I_2(\xi - \xi_0) & \text{if } \xi - \xi_0 > 0 \text{ and } \alpha \geq 0 \\ c_r \alpha \gamma_r I_2(\xi - \xi_0) & \text{if } \xi - \xi_0 \leq 0 \text{ and } \alpha \geq 0 \\ 0 & \text{if } \alpha < 0 \end{cases} \tag{14}$$

where $C_d(\alpha) = c_d$ and $C_r(\alpha) = c_r\alpha$ in Equation 12. This preserves the necessary components for describing the observed slow dynamics while reducing the number of parameters that need to be constrained. In this case, five parameters are related to the damage, that is, ξ_0, γ, c_d, c_r, and the initial strain tensor. It is difficult to constrain all five parameters from the observations by Feng et al. (2018). We choose the parameters following Lyakhovsky et al. (2016) and Lyakhovsky, Reches, et al. (1997). We assume that $\xi_0 = -0.79$ and that the initial strain tensor in 2D is $\varepsilon_{xx0} = -\varepsilon_0$, $\varepsilon_{yy0} = -\varepsilon_0$ and $\varepsilon_{xy0} = \varepsilon_{yx0} = 1.46\varepsilon_0$ such that ξ at the initial strain state satisfies $\xi - \xi_0 < 0$. This enables the damaged rock to heal after removing dynamic perturbations. With the above simplifications, the parameters to be inverted in model L are γ_r, c_d, c_r, and ε_0.

2.2.2.2. *Bayesian Inversion and Uncertainty Quantification (UQ)*

In order to quantify the relative importance of the theoretical model parameters in explaining the evolution of the observed slow dynamics, we apply Bayesian inversion. We first define the required terms to describe the probabilistic distributions of parameters of both models. The model parameters $\underline{m}$ and experimental observations $\underline{d}^{obs}$ are viewed as random variables in $\mathbb{M} \subset \mathbb{R}^{n_m}$ and $\mathbb{D} \subset \mathbb{R}^{n_d}$, where n_m and n_d are the number of model parameters and the number of observed data points.

We then aim to find the posterior, namely the conditional distribution of $\underline{m}$ for a given observation $\underline{d}^{obs}$. We denote the corresponding probability density function (PDF) by $\rho\left(\underline{m}|\underline{d}^{obs}\right)$. We refer to Appendix C for a more detailed description of the Bayesian inversion method that we employ.

To compute an approximation to the posterior distribution, we apply MCMC. Based on the amount of information that we know about the PDEs and the cost of each forward simulation, different types of MCMC sampling algorithms may be chosen. In this work, we choose the AM-MCMC (Haario et al., 2001) algorithm since the forward model simulated with ExaHyPE does not provide the derivatives of the solution with respect to the model parameters. AM-MCMC learns an approximate variance of the posterior on the fly, automatically improving its efficiency during the run by tuning its proposals. While more complex Uncertainty Quantification (UQ) algorithms may achieve higher efficiency, AM-MCMC readily meets our accuracy and computational cost requirements.

We use the AM-MCMC implementation provided by the open-source Massachusetts Institute of Technology Uncertainty Quantification Library (MUQ, Parno et al., 2021). To couple MUQ to the forward model in the ExaHyPE simulation framework, we use the universal UQ/model interface UM-Bridge (Seelinger et al., 2023), which is fully supported by MUQ. For reproducibility, we provide, in the open research section, the forward model as a ready-to-run container image that any UM-Bridge supporting UQ software can connect to.

To ensure that the MCMC method gives a sufficiently good approximation of the inversion results, we compute the Monte Carlo standard error (MCSE) as an indicator (Vehtari et al., 2021). It is defined as

$$\text{MCSE} = \sqrt{\frac{\text{Var}\left(\rho^{MC}\left(\underline{m}|\underline{d}^{obs}\right)\right)}{S}}, \tag{15}$$

where $\rho^{MC}\left(\underline{m}|\underline{d}^{obs}\right)$ is the estimated posterior, Var$(\cdot)$ is the variance of a random variable and S is the number of independent samples drawn from the posterior. MCMC necessarily produces correlated samples, so the effective sample size (ESS) is applied instead of S. The ESS is not immediately available, but can in turn be estimated from the chain's correlated samples (Vehtari et al., 2021). The MCSE estimates are provided by the ArviZ tool (Kumar et al., 2019).

3. Results

In Section 3.1, we show that model B and model L can reproduce the three phases of slow dynamics (Figure 1c). In Section 3.2, we analyze the dependence of the simulated damage on both the frequency and amplitude of perturbations. In Section 3.3, we quantify the uncertainty of each model parameter based on experimental data.

3.1. The Three Phases of Slow Dynamics

As shown in Figure 1c, the change of modulus under cyclic loading experiences three phases from conditioning to recovery. In this section, we explain how models B and L can reproduce the three phases of slow dynamics observed in laboratory experiments. To demonstrate the conditioning and recovery of the damage under dynamic perturbations, we treat the sample in the DAET experiment as an oscillator. We justify the validity of this assumption in Appendix D1. As in Berjamin et al. (2017), we assume that only one strain component ε_{xx} is perturbed. The damage evolution equations for model B are simplified to Equation 16a, and those for model L to Equation 16b, as

$$\dot{\alpha} = \frac{1}{\tau_b \gamma_b}(W - \gamma_b g), \tag{16a}$$

$$\dot{\alpha} = \begin{cases} c_d \exp\left(-\frac{\alpha}{\alpha_d}\right)\gamma_r I_2(\xi - \xi_0) & \text{if } \xi - \xi_0 > 0 \text{ and } \alpha \geq 0 \\ c_r \alpha \gamma_r I_2(\xi - \xi_0) & \text{if } \xi - \xi_0 \leq 0 \text{ and } \alpha \geq 0 \\ 0 & \text{if } \alpha < 0 \end{cases}, \tag{16b}$$

where $W = \left(\frac{1}{2} - \frac{\beta}{3}\varepsilon_{load} - \frac{\delta}{4}\varepsilon_{load}^2\right) M \varepsilon_{load}^2$ in Equation 16a, ε_{load} is the perturbation on ε_{xx} and all other strain components are assumed to be zero. This implies that ε_{load} is $A_0 \sin(2\pi f_c t)$ when $t \leq 10$ s and becomes 0 when $t > 10$ s. In Equation 16b, ξ is computed, using Equation 11, from 2D initial strain with three components ε_{xx0}, ε_{yy0}, and ε_{xy0} plus the perturbation in $\varepsilon_{xx} = \varepsilon_{xx0} + \varepsilon_{load}$ and the remaining strain components are assumed to be zero.

We show the evolution of the damage variables in both models in Figures 3b and 3c. We note here that the conditioning phase of model L (marked with a dashed black curve with an arrow) is subtle in Figure 3b but will be more pronounced if we set c_d to a smaller value in Equation 16b. The parameters are detailed in Table 1. We choose initial strains that satisfy $\xi(\varepsilon_{xx0}, \varepsilon_{yy0}, \varepsilon_{xy0}) - \xi_0 \approx -0.01 < 0$. Both model B (the blue solid curve) and model L (the red solid curve) gradually reach the steady state during perturbations and recover after $\varepsilon_{load} = 0$. In Figure 3b, we also show how the damage will evolve differently when not adding the initial strain or without differentiating the evolution laws for damaging and healing in model L, that is, Equation 16b. Without the initial strain (the red dash-dotted curve), the steady state is reached at a later stage, and larger damage will be induced. More importantly, the accumulated damage does not heal after removing the perturbations. In the case that $\dot{\alpha} = C_d \gamma_r I_2(\xi - \xi_0)$ irrespective of the sign of $\xi - \xi_0$ (the red dashed curve), we observe that no damage accumulates at the end of each cycle. In this case, all damage that accumulated during the damaging phase of a cycle is recovered during the healing phase due to the identical evolution equations.

Figure 3d shows how the change in P-wave velocity relates to the strain perturbations during the stationary phase. We note here that while only the damage evolution of model B doubles the perturbation frequency (highlighted with the two dash-dotted black lines in Figure 3b), both model B and model L generate the "bow-tie" loop that is reported in DAET experiments (Renaud et al., 2012; Rivière et al., 2015, 2016). We will discuss how the "bow-tie" loops form with different mechanisms in Section 4.2.

3.2. Amplitude- and Frequency-Dependent Damage

Both, amplitude- and frequency-dependence of damage have been observed in DAET. Many observations show that the damage at the steady state (marked by the dashed green line with an arrow in Figure 3b) grows with the magnitude and frequency of dynamic perturbations. The amplitude-dependence of damage can be resolved by various models (Aleshin & Van Den Abeele, 2007; Favrie et al., 2015; Vakhnenko et al., 2005); however,

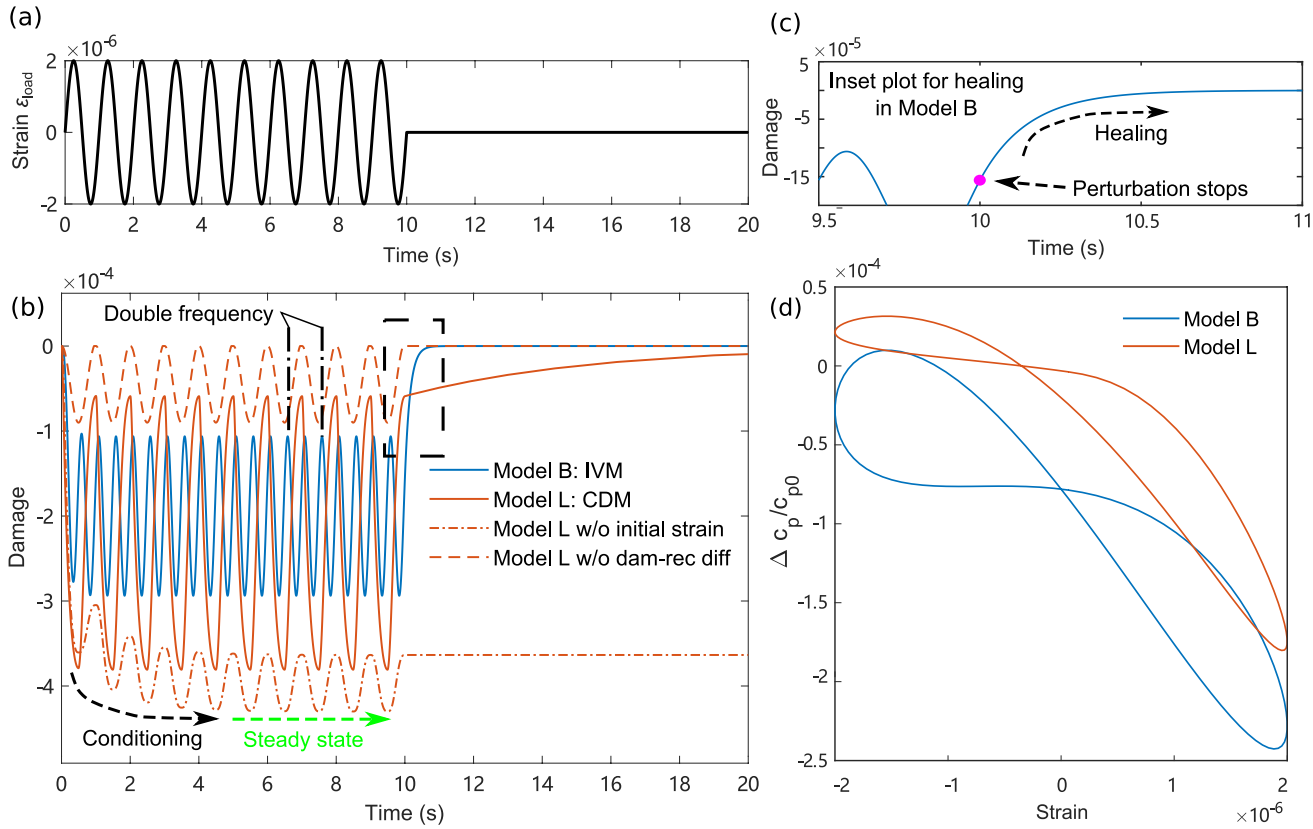

Figure 3. Evolution of the damage variables in model B and model L under a dynamic perturbation that resembles a Dynamic Acousto-elastic Testing experiment. (a) The strain perturbation ε_{load} added to the system. (b) Comparison of the damage conditioning and recovery of model B (blue curve), model L (solid red curve), model L without initial strain (dash-dotted red curve), and model L without different damaging and healing evolution (dashed red curve), that is, $C_d(\alpha) = C_r(\alpha)$ in Equation 12. Model B (Berjamin et al., 2017) is described in Equation 16a, while model L (Lyakhovsky, Ben-Zion, & Agnon, 1997) is described in Equation 16b. The conditioning phase of the models is illustrated with a dashed black curve with an arrow. The steady state evolution phase of the models is illustrated with a dashed green curve with an arrow. The region inside the dashed black rectangle is enlarged in (c) to highlight the healing phase of model B after the perturbation stops (marked with a pink dot). The two vertical, black, dash-dotted lines highlight the doubled frequency during the evolution of damage variable α in model B. (d) Comparison of the change in P-wave speed during one cycle of perturbation after reaching the steady state. $\Delta c_p/c_{p0}$ is the change of P-wave speed Δc_p over the P-wave speed before perturbations c_{p0}.

modeling the frequency dependence of damage remains challenging. The following discussion will focus on the capabilities to also model the frequency-dependent damage in laboratory experiments using models B and L.

Table 1
Summary of Model Parameters for the Comparison of Model B and Model L, With A_0 Being the Amplitude of the Sinusoidal Strain Perturbation, f_c the Frequency of the Strain Perturbation, β the First Order Nonlinearity, δ the Second-Order Nonlinearity, γ_b the Damage Energy, τ_b the Evolution Time Scale, γ_r the Nonlinear Modulus, c_d the Damage Coefficient, c_r the Healing Coefficient, ξ_0 the Modulus Ratio as Defined in Equation 11, c_r Is the Healing Coefficient, ε_{ij0} the Different Components of Initial Strains and α_d the Normalization Factor as Defined in Equation 16b

	Parameters	Values	Units	Parameters	Values	Units
Perturbation	A_0	2×10^{-6}	1	f_c	1.0	Hz
Model B	β	1.0×10^{2}	1	δ	3.0×10^{6}	1
	γ_b	5.0×10^{1}	Pa	τ_b	1.5×10^{-1}	s
Model L	c_d	1.2×10^{-1}	$(\text{Pa}\cdot\text{s})^{-1}$	ε_{xx0}	-1.00×10^{-6}	1
	c_r	5.0×10^{1}	$(\text{Pa}\cdot\text{s})^{-1}$	ε_{yy0}	-1.00×10^{-6}	1
	γ_r	1.6×10^{10}	Pa	ε_{xy0}	1.46×10^{-6}	1
	ξ_0	−0.79	1	α_d	1.0×10^{-4}	1

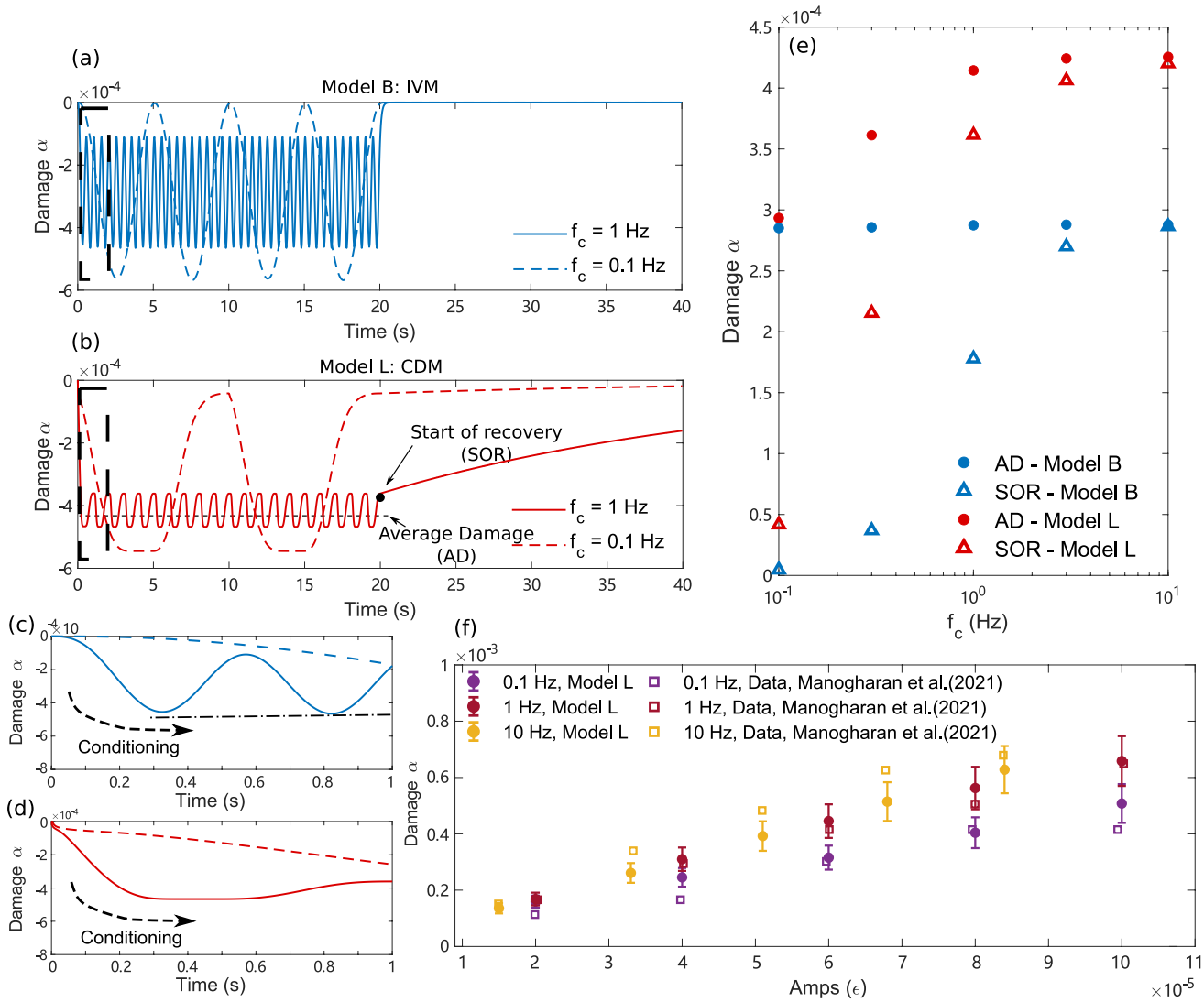

Figure 4. (a) Evolution of the damage variables in model B during dynamic perturbations of a 0.1 Hz (blue dashed curve) and 1 Hz (blue solid curve) source signal. Model B (Berjamin et al., 2017) is described in Equation 16a. The damage evolution at the beginning of perturbations (the region inside the black dashed rectangle) is enlarged in (c) to highlight the conditioning phase. (c) The zoomed-in plot of the region inside the black dashed rectangle in (a). The dash-dotted line shows the peak damage is not reached during the first cycle of perturbations. This indicates that the damage evolution is still in the conditioning phase until ~0.8 s. (b) Evolution of the damage variables in model L during dynamic perturbations of a 0.1 Hz (red dashed curve) and 1 Hz (red solid curve) source. Model L (Lyakhovsky, Ben-Zion, & Agnon, 1997) is described in Equation 16b. The start of recovery (SOR) refers to the damage value at the end of the perturbation and the average damage (AD) refers to the average value of the damage variable at the stationary phase. The damage evolution at the beginning of perturbations (the region inside the black dashed rectangle) is enlarged in (d) to highlight the conditioning phase. (d) The zoomed-in plot of the region inside the black dashed rectangle in (b). (e) Change of AD and SOR at the end of the perturbations under different dynamic perturbation frequencies. The blue dots indicate our results for model B while the green dots are for model L. (f) The change of AD during the stationary phase with the amplitude and the frequency of the perturbations. The rectangles show the AD measured by Manogharan et al. (2021) in their Figure 8g for five different amplitudes and three frequencies (0.1 Hz in purple, 1 Hz in red and 10 Hz in yellow). The colored dots with error bars show our results from model L with the model parameter α_d varying between 0.4 and 0.9 in Table D1. The dots represent the mean values of the model results with varying parameters; while the length of the error bars is the standard deviation of the model results.

We show in Figures 4a–4e how the damage variable α, under two perturbation frequencies (0.1 and 1 Hz), evolves in our numerical simulation using the two models. In model L, both the start of recovery (SOR, annotated in Figure 4b) and the average damage (AD, Figure 4b) during the steady state (Phase 2 in Figure 1c) increase with f_c, which is consistent with the observations from Manogharan et al. (2021, 2022) and Rivière et al. (2016). In model B, SOR follows a similar trend as that in model L. But it shows a frequency independent AD. The difference between SOR and AD damage is usually not explicitly pointed out in the observations regarding the metrics for describing the damage. However, as shown in Figure 4e, they can behave very differently when quantifying

Table 2
Summary of All Model Parameters Considered in the MCMC Inversion, With β Being the First-Order Nonlinearity, δ the Second-Order Nonlinearity, γ_b the Damage Energy, τ_b the Evolution Time Scale, γ_r the Nonlinear Modulus, c_d the Damage Coefficient, c_r the Healing Coefficient, ξ_0 the Modulus Ratio as Defined in Equation 11, c_r the Healing Coefficient and ε_{ij0} the Different Components of Initial Strains

	Param.	Values	Units	Param.	Values	Units
Model B	β	$1.8 \times 10^2 \times [0,4]$	1	δ	$3.0 \times 10^8 \times [0,4]$	1
	γ_b	$1.0 \times 10^{[0,2]}$	Pa	τ_b	$1.0 \times 10^{-6} \times 10^{[0,3]}$	s
Model L	γ_r	$4.5 \times 10^9 \times [0,4]$	Pa	ε_{xx0}	$-\varepsilon_0$	1
	c_d	$1.0 \times 10^5 \times [0,4]$	$(\text{Pa}\cdot\text{s})^{-1}$	ε_{yy0}	$-\varepsilon_0$	1
	c_r	$5.0 \times 10^6 \times 10^{[0,2]}$	$(\text{Pa}\cdot\text{s})^{-1}$	ε_{xy0}	$1.46\varepsilon_0$	1
	ε_0	$5.0 \times 10^{-8} \times 10^{[0,3]}$	1	ξ_0	-0.79	1

the frequency-dependent damage. While AD follows different trends between models B and L, SOR consistently increases with the perturbation frequency in both models.

We note here that the above frequency-dependent behavior of both models results are obtained even when assuming that all nonlinear parameters,that is, β, δ, γ_b, and τ_b in Equation 16a and γ_r, ξ_0, c_d, and c_r in Equation 16b, are frequency-independent. A qualitative explanation of the frequency-dependent SOR can be the following. Under our assumption that the recovery rate increases with the value of the damage variable, stationarity requires a certain level of averaged damage. For higher frequencies, the amplitude of the oscillations of damage in each cycle becomes smaller. This may imply that from the same level of averaged damage, the damage value that the material reaches after one cycle (c.f., the minimum damage) will increase with frequency.

In Figure 4f, we compare the frequency-dependent AD in model L with the measurements by Manogharan et al. (2021) using the model parameters in Table D1. The rectangles show the AD measured by Manogharan et al. (2021) in their Figure 8g for 5 different amplitudes and 3 frequencies (0.1 Hz in purple, 1 Hz in red, and 10 Hz in yellow). The colored dots with error bars show the results from model L with parameters shown in Table D1. The model parameters are varied within certain ranges. The dots represent the mean values of the model results with parameter variations; while the length of error bars is the standard deviation of the model results. We find that most of the measured data points fall within the model predictions and their uncertainties are computed by varying the model parameter as in Table D1. AD increases almost linearly with the amplitude of perturbations (Johnson & Sutin, 2005; Manogharan et al., 2021). The trend of rising damage with higher perturbation frequencies is also captured by model L. We will present a mathematical derivation to explain how model L resolves such frequency-dependent damage in Section 4.1.

3.3. Bayesian Inversion of Damage Model Parameters From Laboratory Observations

In this section, we constrain the behaviors of models B and L with another laboratory experimental set-up—copropagating acousto-elastic testing (Feng et al., 2018). We not only explore the capability of the models in explaining observations but also quantify how well (or badly) model parameters can be constrained from this experiment with the AM-MCMC method introduced in Section 2.2. The values of the parameters to be inverted are of vastly different magnitudes. Thus, normalization is required for the joint sensitivity analysis of all parameters. We assume that the values of σ_M in Equation C2 are 6×10^{-7} and 1×10^{-6}, respectively, for the inversion of model B and model L. The inversion parameters are listed in Table 2.

In the MCMC runs of model B and model L, 70,000 simulations with different model parameters are sampled from the posterior. In this process, 13,826 and 10,444 proposals are accepted, respectively. The MCSE of each parameter in models B and L are given in Figures 6a, 6f, 6k, and 6p. The inversion for each of model B and model L on a single core of the Intel i7-1165G7 processor takes around 10 hr.

We compare the simulation results and the observations from the experiment in Figure 5. We show the raw data of measured modulus changes with dashed red curves. The solid blue curve in Figure 5a and the solid green curve in Figure 5b are, respectively, predictions of model B and model L with the best-fit parameter set in MCMC. Model B (the solid blue curve) and model L (the solid green curve) match the observations with correlation coefficients

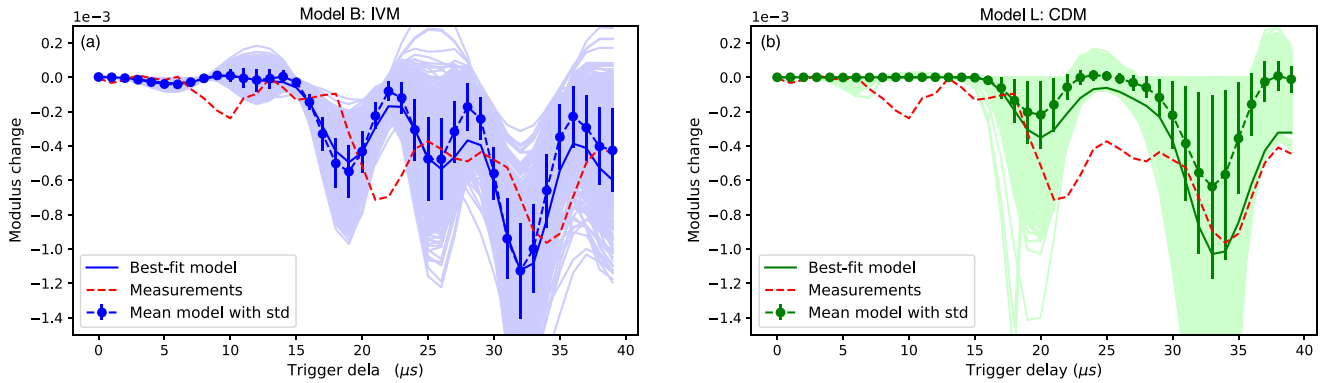

Figure 5. Comparison between the observations from experiments by Feng et al. (2018) and model predictions corresponding to 70,000 Markov chain Monte Carlo samples of the respective model's Bayesian posterior. The data from the experiment is shown with the red dashed line. (a) Inversion results of model B, Equations 13 and 16a. The model prediction with the highest posterior probability is shown in the solid blue curve. The dashed line shows the mean prediction with error bars indicating the standard deviation. All samples' model predictions are plotted as a blue-shaded area. (b) Inversion results of model L, Equation 14. The model prediction with the highest posterior probability is shown in the solid green curve. The dashed line shows the mean prediction with error bars indicating the standard deviation. All samples' model predictions are shown in a green shade.

of 0.91 (model B) and 0.83 (model L). While model B has a higher correlation coefficient, the variation of modulus is delayed compared to the data (the dashed red curve). This time shift is also applied in the visco-elastic formulation proposed by Feng et al. (2018). However, since we here directly simulate the wave propagation and the variation of modulus, needing to add a delay is unexpected.

Unlike model B, if we compare model L and the data in the time interval between 30 and 40 μs, the delay is better resolved. Model L overestimates the modulus increase during the compression of the sample between 20 and 30 μs. The MCMC ensembles of model B (the blue-shaded area) and model L (the green-shaded area) partially account for modulus variation in the early period between 5 and 15 μs. While Feng et al. (2018) achieved a better fit to that earlier part of the signal, their discrepancies between data and model predictions in the later time range, for example, between 30 and 40 μs, were large. We refer to Appendix D2 for a further discussion about the agreement between the model predictions and the experimental data.

The marginal probability distributions of the laboratory-constrained model parameters of models B and L are shown in Figure 6. The histograms in blue on the diagonal of Figure 6 show the one-dimensional marginal distribution of the model parameters in model B. The values with the highest marginal probability for the normalized β, δ, γ_b, and τ_b are 1.10, 3.21, 0.88, and 1.75. The two-dimensional marginal distribution of each pair of two parameters is shown on the upper triangle of Figure 6. The first-order nonlinearity parameter β remains relatively independent of other parameters. In distinction, the correlations among the other three parameters are significantly stronger. We can infer that with higher damage energy (γ_b), the second-order nonlinearity will more likely be larger whereas the time scale for damage evolution τ_b be smaller.

Similarly, the histograms in green on the diagonal of Figure 6 show the one-dimensional marginal distribution of the model parameters in model L. The values with the highest marginal probability for the normalized γ_r, c_d, and ε_0 are 1.30, 0.50, and 1.80. We find that the healing coefficient c_r is not well constrained by the laboratory observations. The two-dimensional marginal distribution of each pair of two parameters is shown on the lower triangle of Figure 6. We observe a negative correlation between the nonlinear modulus γ_r and the damage coefficient c_d. We relate this effect to the lack of resolution in constraining the healing coefficient. According to Figures 6e and 6j, the trend of damage increase due to larger damage coefficient c_d is better compensated for by the decrease of the nonlinear modulus γ_r than by the increase of the healing coefficient c_r.

We here summarize the information gained from this section. We can estimate the following parameters from the data in co-propagating acousto-elastic testing: the first-order nonlinearity (β), the second-order nonlinearity (δ), and the damage energy (γ_b) in model B, as well as the nonlinear modulus (γ), the damage coefficient (c_d), and the initial strain level (ε_0) in model L. Among them, the initial strain level (ε_0) is an important parameter that we introduce in this paper to explain slow dynamics as shown by the dash-dotted red curve in Figure 3b. We will discuss the physical implications of this parameter in Section 4.3. Two model parameters are poorly constrained—the

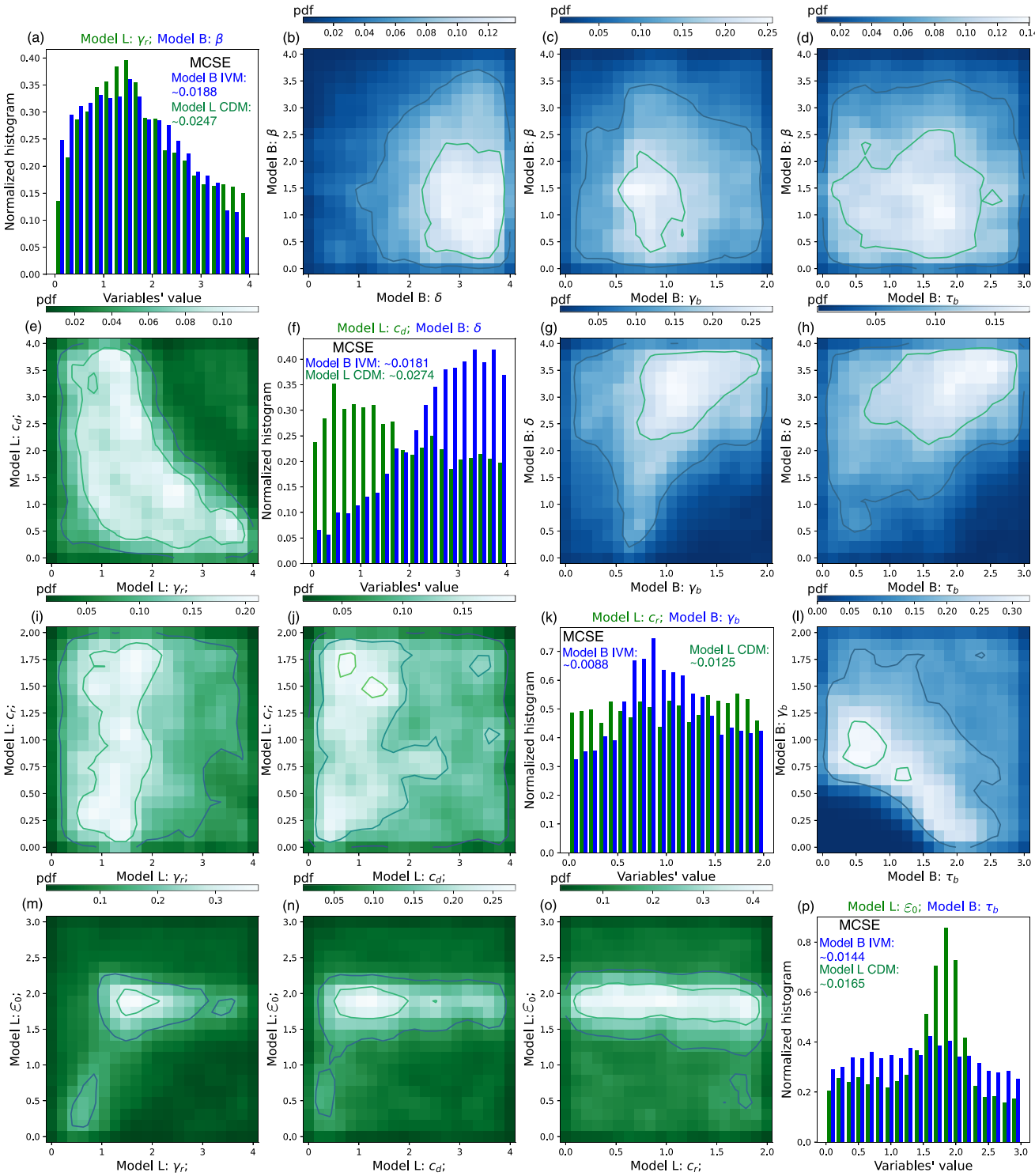

Figure 6. Sensitivity of different parameters in model B and in model L based on Markov chain Monte Carlo inversion. We show the one-dimensional marginal probability density of the four parameters in model B (in blue) and model L (in green) on the diagonal of the plot matrix. The four parameters in model B from left to right and top to bottom are the first-order nonlinearity (β), the second-order nonlinearity (δ), the damage energy (γ_b), and the evolution time scale (τ_b). The four parameters in model L from left to right and top to bottom are the nonlinear modulus (γ), the damage coefficient (c_d), the healing coefficient (c_r) and the initial strain level (ε_0). The two-dimensional marginal probability density of all pairs of two parameters in model B is shown in the upper triangle subplots of the plot matrix. The density is shown with the color map from dark blue to white. The brighter the color, the higher the density. Similarly, the two-dimensional marginal probability density of all pairs of two parameters in model L is shown in the lower triangle subplots of the plot matrix. The density is shown with the color map from dark green to white. The brighter the color, the higher the density. MCSE stands for Monte Carlo standard errors of each model parameter.

evolution time scale (τ_b) in model B, and the healing coefficient (c_r) in model L. We will discuss possible reasons and suggest feasible ways to better constrain these parameters in Section 4.4.

4. Discussion

In this paper, we analyze the behavior of two physical models to simulate nonlinear elastic wave propagation and compare them with laboratory observations. Several interesting aspects are worth further discussing here: (a) We find that model L can reproduce the increase of AD with the frequency of strain perturbations during the steady state of damage. We will here revisit this main advantage and interpret it from both mathematical and physical points of view. (b) We will also discuss how the influence of the damage variable on the wave speeds can be similar to second-order nonlinearity. (c) In model L, one of the key assumptions required for recovery after removing perturbations is the existence of initial strain. We will discuss the validity of this assumption. (d) Most importantly, we will revisit the major goal of proposing models whose parameters can be constrained. This enables the models to be applied to connect the observed non-classical nonlinearity in the laboratory and in the field.

4.1. The Frequency-Dependence of Damage

Recent studies find a general trend of increasing AD with the excitation frequency during the stationary phase (Manogharan et al., 2021, 2022; Rivière et al., 2016). However, the underlying mechanism is not well understood. While Rivière et al. (2016) favors models with rate/time dependencies, not every such model also results in frequency-dependent damage during the steady state. In model B, the AD is $\frac{E}{4\gamma_b}A^2 + \mathcal{O}\left(A^4\right)$ (Berjamin et al., 2017), where A is the strain amplitude of perturbations and is not related to the frequency (see also Figure 4). In model L, frequency-dependent AD is observed and follows the same trend as the measurements (c.f., the red dots in Figure 4e).

We here interpret these findings analytically (see Appendix A1). We show that in model L, the decrease of the damage coefficient and the increase of the healing coefficient with damage contribute differently to the frequency-dependent AD. We can also show that damage at the steady state can increase with the frequency of the dynamic perturbation. Specifically, with increasing healing coefficient ($C_r(\alpha) = c_r\alpha$), the AD tends to decrease with frequency, that is, Equation A2; while with decreasing damage coefficient ($C_d(\alpha) = c_d \exp(\alpha/\alpha_d)$), AD becomes larger as the frequency increases, that is, Equation A6.

4.2. Damage Versus Second-Order Nonlinearity Contributions to Co-Seismic Changes in Wave Speed

Forming a "bow-tie" loop relation between the wave speed variation and the strain perturbation requires that the time series of the modulus change contain a frequency component that doubles the frequency of strain oscillation. In model B, there are two sources of such double frequency. The first mechanism is second-order nonlinearity, as has been recognized in previous analysis (Sens-Schönfelder et al., 2019). The second mechanism contributing to the double frequency is related to damage and healing within a cycle. The rock is damaged when the absolute value of the strain increases while it heals otherwise. This leads to two cycles of damage and healing inside one cycle of strain perturbation.

In model L, neither the second-order nonlinearity (δ) nor the double damage-healing cycles exist. The rock damages when the tensile strain is large enough that $\xi - \xi_0 > 0$ and it heals otherwise. This implies that the oscillation of the damage variable has the same frequency as the strain perturbations, as highlighted with the two dash-dotted black lines in Figure 3b. Instead, the mechanism in model L that adds the double frequency to the damage evolution is the change of wave speed with the amplitude of the strain, coming from the third non-quadratic term in Equation 10.

We caution that damage effects may be confused with the effects of second-order nonlinearity in observations of "bow-tie" loops. In the framework of this paper, we introduce a damage variable to explain the conditioning and the recovery of the wave speed. However, in addition to slow dynamics, the damage variable can also influence the measured wave speed in a similar way as classical nonlinearity. Such confusion may also appear in comparisons of modulus variation as in Figure 6. The third parameter (the damage energy γ_b) in model B determines the magnitude of damage: the smaller the damage energy, the larger the magnitude of the damage. We conclude that the positive correlation between γ_b and the second-order nonlinearity (δ) implies that the effect of the damage

evolution on the modulus is comparable to that of the second-order nonlinearity. However, it is possible to discern the fundamental difference in the effects of the damage variable versus second-order (classical) nonlinearity. The latter will lead to the same strain-dependent modulus change, irrespective of the loading rate. However, the change of modulus due to the damage variable will always be rate-dependent, as given in Equation 6.

4.3. Physical Interpretation of Both Damage Models

Whether damage evolution discriminates between compression and extension can lead to different interpretations of the physical mechanisms underlying the evolution of the damage variables. Different hypotheses have been proposed relating damage to friction (Aleshin & Van Den Abeele, 2007) or to adhesion (Lebedev & Ostrovsky, 2014). Since the sign of $\gamma_b g$ in Equation 8 is not related to compression or extension of strain, the healing and damage terms of model B are clearly separated. The healing term becomes larger than zero once damage occurs irrespective of the strain state. The healing term is simultaneously increasing with the accumulation of damage. Once the healing term becomes large enough, damage accumulation reaches a steady state.

In contrast, the damage evolution of the material in model L differentiates between compressive and extensional deformation. Here, rock only heals when the material is sufficiently compressed ($\xi - \xi_0 < 0$). The quasi-static state is reached due to increasing healing speed. Lebedev and Ostrovsky (2014) have proposed a possible explanation of slow dynamics being related to the thermal processes due to adhesion at the contacts of rock grains. The adhesion potential (Jacob & Israelachvili, 1992) is non-symmetric for compression and extension. The mechanism of adhesion therefore also favors a model that considers different effects of damage and healing under compression and extension.

While both models explain the slow dynamics mathematically, the physical interpretation of model L has richer physical implications. First, each term in the internal energy of model L has a physical meaning, and the formulation strictly follows the laws of thermodynamics. The healing is related to $\gamma I_1 \sqrt{I_2}$, a term that comes from the opening and closing of micro-cracks (Lyakhovsky, Ben-Zion, & Agnon, 1997). At the microscopic scale, this may be interpreted as a re-attachment of asperities at contact surfaces. Second, as shown in Figure 6, the initial strain is relatively well resolved to be around 3×10^{-6}. The existence of this non-negligible initial strain may be related to the cohesive contact or to the thermal deformation of rocks. The typical thermal expansion coefficient of rock is of the order of 10^{-5} K^{-1} (Kirk & Williamson, 2012), where K is the unit of the absolute temperature. This means a change of less than 1 K may equate to the here-constrained magnitude of the initial strain. Although more observations are required to confirm this interpretation, the existence of initial strain possibly explains why slow dynamics typically become prominent when the dynamic strain is larger than 10^{-6} but not for smaller values (Remillieux et al., 2017). Gajst (2020) and Lyakhovsky et al. (2022) add a storage energy term in model L that is similar to the second term in Equation 8. This new term also prevents the growth of damage until the perturbation is larger than a certain threshold. Whether introducing an initial strain as in our work or adding an additional storage energy term is more suitable for explaining the observed non-classical nonlinearity discussed in this paper is an interesting topic for future work.

We also note that the steady state is reached due to the increasing speed of healing under compression with a larger accumulated damage. This increase is not necessarily linear. It is here only assumed to be linear in Equation 14 for simplicity and demonstration purposes. A physically motivated expression requires specific experiments to constrain this behavior.

4.4. Model Complexities and Data Availability

In the following, we discuss current limitations and future avenues for constraining parameters in models B and L from experiments. We will argue for the potential of conducting DAET and copropagating acousto-elastic testing experiments on the same sample to more accurately invert the model parameters.

β and δ in Equation 13 of model B, and γ_r and ε_0 in Equation 14 of model L are related to the simultaneous oscillation of modulus with the cyclic loading in Phase 2 of slow dynamics in Figure 1. In the copropagating acousto-elastic testing experiments, the wavefront of the probing wave is propagating simultaneously with the wavefront of the pump wave. Thus, we can use this experiment to constrain β and δ in model B and γ_r, ε_0 in model L, see Figures 6a, 6f, and 6p.

However, since the duration of perturbation in the copropagating acousto-elastic testing experiments is not long enough, τ_b in Equation 13 of model B, c_d and c_r in Equation 14 of model L are less well constrained in Figures 6f, 6k, and 6p. As explained in Section 3.1, τ_b and γ_b of model B, as well as c_d and c_r of model L, describe how the models reproduce the mechanical response of rock samples at a longer time scale. In this work, we use DAET experiments to estimate these model parameters in Figure 4f. However, for the same sample, no co-propagating acousto-elastic testing experiment is available. Longer time scale damage model parameters may be better constrained using DAET and copropagating acousto-elastic testing experiments on the same sample.

4.5. Limitations

The damage variable capsulizes changes in material stress-strain relations due to the physical processes, such as adhesion (Lebedev & Ostrovsky, 2014), plastic deformation at grain contacts (Lieou et al., 2017), or friction (Aleshin & Van Den Abeele, 2007) at meso- and microscopic scales. Compared to the explanation of Lebedev and Ostrovsky (2014), the accumulation of damage during the extension of material might be related to the detachment at the contacts of asperities; whereas the recovery (decrease of the damage variable value) might be associated with re-attachment and with asperities that gradually shift from the secondary stationary state to the main stationary state. However, developing a stringent mathematical framework connecting the damage variable at the macroscopic scale with microscopic physical processes is challenging and currently elusive.

Model L does not match the modulus change equally well as model B, especially during rock compression. In model L, the increase in wave speed due to the third term $\gamma I_1 \sqrt{I_2}$ during compression cancels out the wave-speed drop from damage. Future modification of model L may mitigate the influence of its third term on the change in wave speed while preserving the differentiation between tensile and compressive strains.

In this work, we analyze the behaviors of two damage models. To compare our 2D simulation results with laboratory observations, we simplify some of the model parameters, acknowledging the limited amount of available observational data. One aspect that will require further investigation for modeling slow dynamics in 2D and 3D is the full response of material damage from strain perturbations, including different components of the strain/stress tensor. Lott et al. (2017) proposed a formulation that connects a scalar damage variable to the stiffness tensor. The resulting changes in P- and S-wave speed in response to different modes of perturbations qualitatively match observations. In future work, this relationship may be combined into the internal energy formulation in Equation 2 to potentially refine our dynamic understanding of how the steady state in DAET (Phase 2 in Figure 1) is reached.

The achieved quantitative match of our modeling results and laboratory observations demonstrates the potential of both proposed models to capture natural co-seismic damage of rocks. The amplitudes of the changes in moduli modeled here and observed in laboratory experiments are small under small strain perturbations ($\sim 10^{-4}$, see Tables 1 and 2, and Figure 4f). At the field scale, the observed magnitudes of moduli changes vary between 10^{-4} and 10^{-1} depending on the depth, rock/soil types, and level of the dynamic strain (e.g., Gassenmeier et al., 2016; Qin et al., 2020; Wang et al., 2021). As a next step, the nonlinear models can be implemented in large-scale 3D wave solvers, for example, SeisSol (https://seissol.org) or ExaHyPE (Reinarz et al., 2020). The associated major challenges stem from the nature of nonlinear hyperbolic PDEs. Solutions can become discontinuous during the propagation of waves even when the initial conditions are smooth (LeVeque, 2002). There are numerical methods that may resolve such dynamic discontinuities by introducing numerical diffusion. This comes with different criteria for numerical stability and typically requires higher spatial and temporal resolution. It leads to computationally more expensive schemes. However, to simulate co-seismic damage and post-seismic recovery as observed in the field, 3D simulations will be indispensable to help bridge the gap between the laboratory and the field scales.

5. Conclusions

We demonstrate the applicability of two models that explain the observed non-classical nonlinear behaviors of rocks, an IVM and a continuum damage model (CDM). The analyzed IVM, model B, is proposed by Berjamin et al. (2017), while the CDM, model L, is adapted from Lyakhovsky, Ben-Zion, and Agnon (1997). Using both physical models, we numerically simulate nonlinear wave propagation in rocks with fast and slow dynamics with the DG method in 2D.

- We compare the simulation results with two sets of experiments. In DAET, the model that we adapted from Lyakhovsky, Ben-Zion, and Agnon (1997) can quantitatively explain both amplitude- and frequency-dependent damage of rock samples;
- In co-propagating acousto-elastic testing, the change of modulus in laboratory observation has a higher correlation coefficient with simulation results using the model by Berjamin et al. (2017) than those of the model that we adapted from Lyakhovsky, Ben-Zion, and Agnon (1997). However, only the latter model explains the observed delay of modulus variation relative to strain;
- From the joint posterior distribution of the model's parameter space using AM-MCMC, we demonstrate that nonlinear parameters can be resolved but that the associated uncertainties vary. We find that the effects on wave-speed changes from the second-order nonlinearity and from the damage variable can be very similar;
- The evolution time scale (τ_b) in the model of Berjamin et al. (2017) and the healing coefficients c_r in the adapted model from Lyakhovsky, Ben-Zion, and Agnon (1997) are particularly challenging to resolve from co-propagating acousto-elastic testing. We suggest that the model parameters can be better constrained if we can conduct DAET and copropagating acousto-elastic testing on the same sample.

We conclude that the quantitative match between both models and the laboratory observations justifies the applicability of these models in describing the phenomena of slow dynamics. Future nonlinear damage modeling using either physical model in a 3D highly-scalable software for seismic wave propagation simulations will allow comparison to field-scale observations and account for natural complexities such as complex surface topography and subsurface heterogeneities.

Appendix A: Analytical Analysis of Model L

A1. Analytical Interpretation of the Frequency Dependence of Model L

Here we derive analytical solutions to the frequency-dependent damage of the model of Lyakhovsky, Ben-Zion, and Agnon (1997). We make the following simplifying assumptions: First, we assume that only ε_{xx} is perturbed by $\varepsilon_{load} = \varepsilon_0 \sin(\omega_c t)$, as in Figure 3. As in Table 1, $\xi\left(\underset{=}{\varepsilon_0}\right) + \xi \approx 0.01$ and is assumed to be zero at the initial strain level. Further, we approximate $I_2(\xi - \xi_0) = R_0\varepsilon_{load} + \mathcal{O}\left(\varepsilon_{load}^2\right) \approx R_0\varepsilon_{load}$.

A1.1. Increasing Healing Coefficient With Damage

In the case when the healing coefficient linearly increases with the damage variable, Equation 12 is simplified as

$$\dot{\alpha} = \begin{cases} C_d\gamma_r R_0\varepsilon_{load} = \frac{c_1}{\varepsilon_0}\varepsilon_{load} & \text{if } \varepsilon_{load} > 0 \text{ and } \alpha \geq 0 \\ C_r\alpha\gamma_r R_0\varepsilon_{load} = \frac{k_1}{\varepsilon_0}\alpha\varepsilon_{load} & \text{if } e\varepsilon_{load} \leq 0 \text{ and } \alpha \geq 0 \cdot \\ 0 & \text{if } \alpha < 0 \end{cases} \tag{A1}$$

Consider one cycle of perturbation where $t \in [0, 2\pi/\omega_c]$ and the damage variable at the beginning of the cycle is α_0. We then derive that the maximum damage at $t = \pi/\omega_c$ is $\alpha_{\max} = \alpha_0 + 2c_1/\omega_c$ at the end of the cycle, $\alpha_t = \alpha_{\max} \exp(-2k_1/\omega_c)$. At the dynamically steady state, $\alpha_t = \alpha_0$. The average of the damage variable in a cycle is approximated by

$$<\alpha> \approx 0.5(\alpha_0 + \alpha_{\max}) = \frac{c_1}{\omega_c}\frac{1 + \varepsilon_{load}^{-2k_1/\omega_c}}{1 - \varepsilon_{load}^{-2k_1/\omega_c}}, \tag{A2}$$

which is monotonously decreasing with frequency.

A1.2. Decreasing Damaging Coefficient With Damage

In the case when the damage coefficient exponentially decreases with the damage variable, Equation 12 is simplified as

$$\dot{\alpha} = \begin{cases} C_d \gamma_r R_0 \exp(-\alpha/\alpha_d)\varepsilon_{load} = \frac{c_1}{\varepsilon_0}\exp(-\alpha/\alpha_d)\varepsilon_{load} & \text{if } \varepsilon_{load} > 0 \text{ and } \alpha \geq 0 \\ C_r \gamma_r R_0 \varepsilon_{load} = \frac{c_2}{\varepsilon_0}\varepsilon_{load} & \text{if } \varepsilon_{load} \leq 0 \text{ and } \alpha \geq 0 \\ 0 & \text{if } \alpha < 0 \end{cases}. \tag{A3}$$

Following a similar consideration as above, we derive

$$\exp(\alpha_0/\alpha_d) = \frac{K}{1-K}\frac{2c_1}{\omega_c \alpha_d}, \tag{A4}$$

$$\exp(\alpha_{\max}/\alpha_d) = \exp(\alpha_0/\alpha_d) + \frac{2c_1}{\alpha_d \omega_c}, \tag{A5}$$

where $K = \exp\left(-\frac{2c_2}{\alpha_d \omega_c}\right)$. Multiplying Equations A4 and A5, it is derived that

$$\exp\left(\frac{\alpha_0 + \alpha_{\max}}{\alpha_d}\right) = \frac{K}{(1-K)^2}\left(\frac{2c_1}{\omega_c \alpha_d}\right)^2. \tag{A6}$$

with the right-hand side monotonously increasing with frequency.

Analytical analysis of the combination of the two cases in Equations A1 and A3 is challenging. But within the parameter space used in Figure 4, we can show that the damage at the steady state can increase with the frequency of the dynamic perturbation.

A2. Model L in 2D

The model of Lyakhovsky, Ben-Zion, and Agnon (1997), with plane strain assumption, can be written in 2D as a set of hyperbolic PDEs as

$$\frac{\partial \underline{q}}{\partial t} = \frac{\partial \underline{F}}{\partial x} + \frac{\partial \underline{G}}{\partial y} + \underline{s}, \tag{A7}$$

where

$$\underline{q} = (\varepsilon_{xx}, \varepsilon_{yy}, \varepsilon_{xy}, v_x, v_y, \alpha)^T,$$
$$\underline{F} = \left(v_x, 0, \frac{1}{2}v_y, \sigma_{xx}/\rho, \sigma_{xy}/\rho, 0\right)^T,$$
$$\underline{G} = \left(0, v_y, \frac{1}{2}v_x, \sigma_{xy}/\rho, \sigma_{yy}/\rho, 0\right)^T,$$
$$\underline{s} = \left(0, 0, 0, 0, 0, \dot{\alpha}\right),$$

and $\dot{\alpha}$ is given in Equation 12. The stress-strain relationship is $\sigma_{ij} = \left(\lambda I_1 - \gamma\sqrt{I_2}\right)\delta_{ij} + \left(2\mu - \gamma\frac{I_1}{\sqrt{I_2}}\right)\varepsilon_{ij}$. It is therefore derived that

$$\frac{\partial \underline{F}}{\partial \underline{q}} = \begin{bmatrix} 0 & 0 & 0 & 0 & 1 & 0 & 0 \\ 0 & 0 & 0 & 0 & 0 & 0 & 0 \\ 0 & 0 & 0 & 0 & 0 & 1/2 & 0 \\ Q_{11} & Q_{12} & Q_{13} & 0 & 0 & 0 & D_1 \\ Q_{21} & Q_{22} & Q_{23} & 0 & 0 & 0 & D_2 \\ 0 & 0 & 0 & 0 & 0 & 0 & 0 \end{bmatrix}, \tag{A8}$$

where

$$\rho Q_{11} = (\lambda + 2\mu) - \gamma\left(2\frac{\varepsilon_{xx}}{\sqrt{I_2}} + \frac{I_1\left(\varepsilon_{yy}^2 + 2\varepsilon_{xy}^2\right)}{I_2\sqrt{I_2}}\right),$$
$$\rho Q_{12} = \lambda - \gamma\left(\frac{I_1}{\sqrt{I_2}} - \frac{I_1\varepsilon_{xx}\varepsilon_{yy}}{I_2\sqrt{I_2}}\right),$$
$$\rho Q_{13} = -\gamma\left(\frac{2\varepsilon_{xy}}{\sqrt{I_2}} - \frac{2I_1\varepsilon_{xx}\varepsilon_{xy}}{I_2\sqrt{I_2}}\right),$$
$$\rho Q_{21} = -\gamma\left(\frac{\varepsilon_{xy}}{\sqrt{I_2}} - \frac{I_1\varepsilon_{xx}\varepsilon_{xy}}{I_2\sqrt{I_2}}\right),$$
$$\rho Q_{22} = -\gamma\left(\frac{\varepsilon_{xy}}{\sqrt{I_2}} - \frac{I_1\varepsilon_{yy}\varepsilon_{xy}}{I_2\sqrt{I_2}}\right),$$
$$\rho Q_{23} = 2\mu - \gamma I_1\frac{\varepsilon_{xx}^2 + \varepsilon_{yy}^2}{I_2\sqrt{I_2}}.$$

With the same method as in Berjamin et al. (2019), the P-wave velocity in the x direction reads

$$c_p = \frac{1}{2}\sqrt{2Q_{11} + Q_{23} + \sqrt{(2Q_{11} - Q_{23})^2 + 8Q_{13}Q_{21}}}, \tag{A9}$$

Appendix B: Numerical Implementation and Verification in ExaHyPE

In this verification benchmark, the simulation domain is [0.0, 0.4] m × [0.0, 0.4] m. A point force radiates seismic waves and is defined as $f_x = A\sin 2\pi f_c t\delta(x - x_s)\delta(y - y_s)$, where δ is the Dirac delta function injected at (0.2, 0.2) m in x-direction and $f_c = 100$ Hz. Following the implementation of Berjamin et al. (2019), the Dirac delta function is approximated as

$$\delta(x - x_s)\delta(y - y_s) = \frac{\exp\left(-(d/\sigma_c)^2\right)}{\pi\sigma_c^2\left(1 - \exp\left(-(R/\sigma_c)^2\right)\right)}\mathbf{1}_{d\le R}, \tag{B1}$$

where $d = \sqrt{(x - x_s)^2 + (y - y_s)^2}$; $\mathbf{1}_{d\le R}$ is the indicator function whose support is a disk space with a radius of $R = c_p/(7.5f_c)$; $c_p = \sqrt{(\lambda + 2\mu)/rho_0}$ is the speed of the P-wave in the undamaged material and the width parameter of the Gaussian function is $\sigma_c = R/2$. In the simulation using the ADER-DG method in ExaHyPE, a structured quadrilateral computational mesh is used to discretize the space with an element edge length of around 1.66 mm, which means that 27 cells resolve one wavelength of P waves and 16 cells resolve one wavelength of S waves. We choose the first order Lagrange basis with Gauss-Legendre quadrature nodes. The achieved excellent agreement is shown in Figure B1. Figure B1a shows the map of elastic strain energy at $t = 0.04$ ms from Berjamin et al. (2019). Solutions to the damage (α) evolution at the two receivers, R1 at (0.2, 0.22) m and R2 at (0.2, 0.27) m are compared between the Finite Volume solutions of Berjamin et al. (2019) and our implementation in ExaHyPE in Figures B1b and B1c.

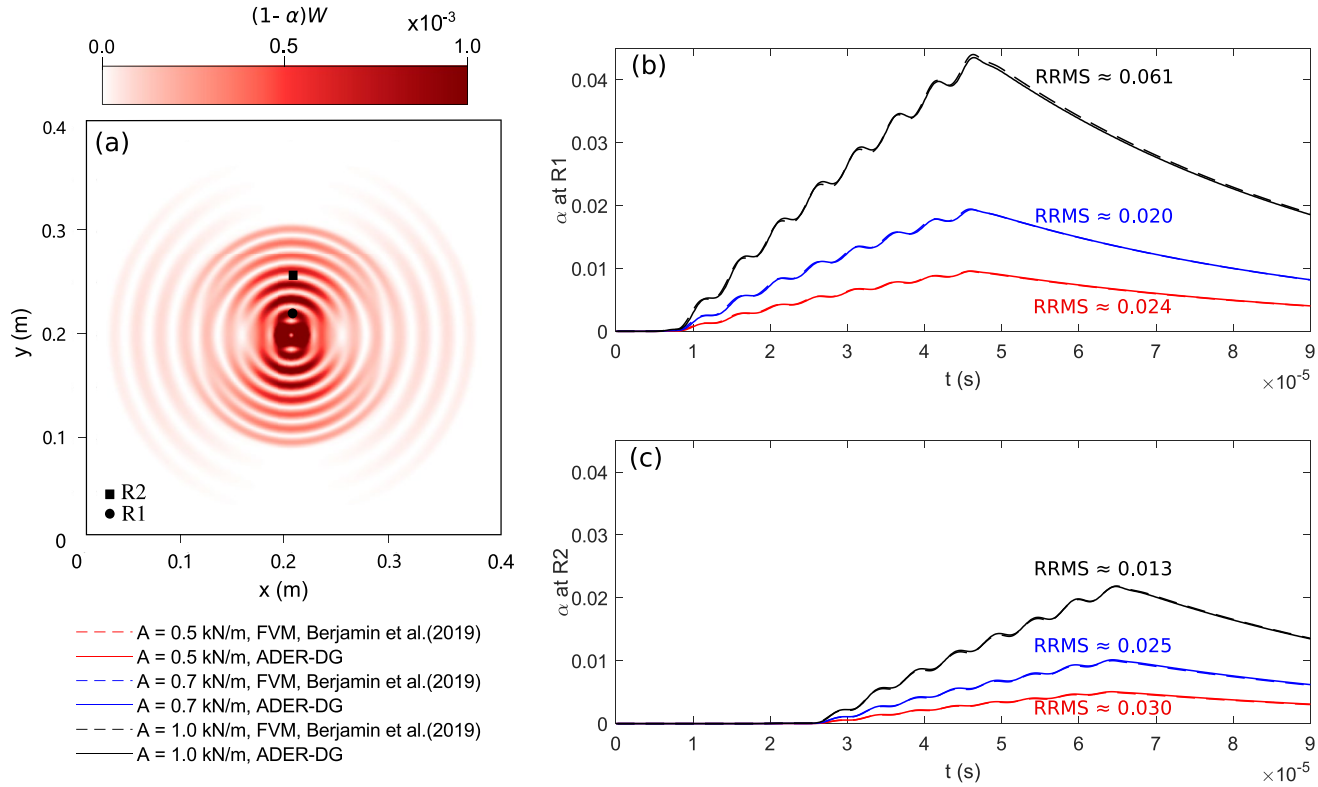

Figure B1. (a) Snapshot of the elastic strain energy field $(1-\alpha)W$ in J/m^3 at $t = 0.04$ ms by Berjamin et al. (2019) simulated using the Finite Volume Method (FVM). R1 at (0.2, 0.22) m and R2 at (0.2, 0.27) m are the locations of two receivers where the recorded time series of the damage variable α is shown in (b) and (c), respectively. The solutions from Berjamin et al. (2019) with FVM are plotted as dashed curves and the ExaHyPE solutions of our implementation with the arbitrary high-order discontinuous Galerkin (ADER-DG) method are plotted in solid curves for R1 in (b) and R2 in (c). Different source amplitudes with $A = 0.5$, 0.7, and 1.0 kN/m are plotted in red, blue, and black, respectively. The relative root mean square errors $= \sqrt{(\boldsymbol{\alpha_1} - \boldsymbol{\alpha_2})^2 / \left(\boldsymbol{\alpha_2} - \bar{\boldsymbol{\alpha}}_{\boldsymbol{2}}\right)^2}$, derived from the solution vectors of ADER-DG $\boldsymbol{\alpha_1}$ and FVM $\boldsymbol{\alpha_2}$ respectively, are denoted and $\bar{\boldsymbol{\alpha}}_{\boldsymbol{2}}$ is the average of $\boldsymbol{\alpha_2}$.

Appendix C: Theoretical Background for Bayesian Inversion

In order to quantitatively investigate the relative importance of the theoretical model parameters that explain the evolution of the observed slow dynamics, we apply Bayesian inversion to both models.

The model parameters $\underline{m}$ and experimental observations $\underline{d}^{obs}$ are viewed as random variables in $\mathbb{M} \subset \mathbb{R}^{n_m}$ and $\mathbb{D} \subset \mathbb{R}^{n_d}$, where n_m and n_d are the number of model parameters and the number of observed data points. Let $G : \mathbb{R}^{n_m} \to \mathbb{R}^{n_d}$ denote the model map taking a parameter onto a model prediction.

We then aim to find the posterior, namely the conditional distribution of $\underline{m}$ for a given observation $\underline{d}^{obs}$. We denote the corresponding PDF by $\rho\left(\underline{m}|\underline{d}^{obs}\right)$. To directly compute underlying parameters from observed data, we would have to apply the inverse of the model map G^{-1}. However, that inverse is not available for our models. Employing Bayes' theorem, we can reformulate the posterior in a way that, as will be detailed below, only involves the forward map G:

$$\rho\left(\underline{m}|\underline{d}^{obs}\right) = \frac{\rho\left(\underline{d}^{obs}|\underline{m}\right)\rho\left(\underline{m}\right)}{\rho\left(\underline{d}^{obs}\right)} \propto \rho\left(\underline{d}^{obs}|\underline{m}\right)\rho\left(\underline{m}\right). \tag{C1}$$

We call $\rho\left(\underline{m}\right)$ the prior density, $\rho\left(\underline{d}^{obs}|\underline{m}\right)$ is the likelihood that describes the probability density of measuring the observed data when $\underline{m}$ is given, and $\rho\left(\underline{d}^{obs}\right)$ is the unconditional PDF of measuring the observed data. Broadly speaking, the posterior considers a model parameter to be likely if the parameter is plausible and its corresponding model prediction is close to observed data.

In practice, $\rho\left(\underline{d}^{obs}\right)$ is not available. A way to circumvent an analytical derivation is to sample the posterior with the MCMC method, where $\rho\left(\underline{d}^{obs}\right)$ cancels out due to being independent of $\underline{m}$.

The prior encodes expert knowledge about what parameters might be generally plausible, not considering our specific observation. Considering the physical constraint that all model parameters are non-negative, it is $\mathbb{M} = \left\{\underline{m} \in \mathbb{R}^{n_m} | 0 \le m_i \le b_i, i = 1, 2, \ldots, n_m\right\}$. b_i is the assumed upper bounds of each model parameter. Another constraint on the model parameters is $\int_{\mathbb{M}} \rho\left(\underline{m}\right) d\underline{m} = 1$. With the above two constraints and based on the maximum entropy principle of designing the prior (Good, 1963), the data is assumed to be uniformly distributed in $\mathbb{M}$.

Since we assume measurement errors to be Gaussian, we choose the likelihood as a Gaussian distribution centered around the model prediction $G\left(\underline{m}\right)$:

$$\rho\left(\underline{d}^{obs}|\underline{m}\right) = \frac{1}{\sqrt{(2\pi)^n \det \underline{\underline{C}}}} e^{-\frac{1}{2}\left(\underline{d}^{obs} - G\left(\underline{m}\right)\right)^T \underline{\underline{C}}^{-1}\left(\underline{d}^{obs} - G\left(\underline{m}\right)\right)}. \tag{C2}$$

The covariance matrix $\underline{\underline{C}} \in \mathbb{R}^{n_d \times n_d}$ captures the assumed variances of and the correlation between data points, encoding our knowledge about measurement accuracy. With the additional assumption that the measurements of data points are independent of each other and all have the same variance σ_m^2, we set $\underline{\underline{C}} = \mathrm{diag}\left(\sigma_m^2, \ldots, \sigma_m^2\right)$.

From Equations C1 and C2 it is clear that the posterior density can, up to an unknown constant factor, be computed point-wise. Every evaluation then requires a corresponding evaluation of the model map, that is, one simulation run.

Appendix D: Details About the Comparison With the DAET Experiments

D1. The Validity of Treating a DAET Sample as a 0D Oscillator

Manogharan et al. (2021) conduct DAET measurements on Westerly granite rock samples under triaxial loading conditions. They load the sample with 20 cycles of sinusoidal stress perturbations in one direction. The loading frequencies are 0.1, 1, and 10 Hz. For each frequency, they load the sample with 5 different amplitudes. They monitor the change of P-wave speeds during the oscillations and after the oscillation stops.

Before looking into details of the results, we first justify the validity of assuming the sample in DAET as an oscillator under the used loading frequencies. The shortest wavelength of P-wave in their rock sample is around 4,165 m/s/10 Hz ≈ 416.5 m (Manogharan et al., 2021). This is still much larger than the length of the sample, which is 26 mm in the direction of loading. If we further assume the material is homogeneous, the strain field induced by the pumping signals is then uniform. This also means we can ignore the propagation of the pumping waves. In other words, we treat the sample as an oscillator.

D2. Agreement Between the Model Predictions and the Experimental Data in Figure 5

We here extend the discussion in Section 3.3 of the main text. We first give an explanation to how model L explains the delay. In Equation 11, when the tensile strain reaches its peak, damage development will not cease ($\xi - \xi_0 > 0$). It only stops upon the strain becoming sufficiently compressive, that is, once ξ is much smaller than zero such that $\xi - \xi_0 < 0$. This further damage that lasts for around 1/4 of the cycle leads to a larger modulus drop after peak tensile stress as is observed in the laboratory data. However, between 20 and 30 μs, there is a

discrepancy between the solid green curve and the dashed red curve. The strain within this time range is negative (compressive). This indicates that model L overestimates the modulus increase during the compression of the sample.

Between 5 and 15 μs, both model B (the solid blue curve) and model L (the solid green curve) do not vary as much as the data. However, the MCMC ensembles of model B (the blue-shaded area) and model L (the green-shaded area) account for modulus variation at that early period. The early modulus drops are compromised in our inversion to fit the later part of the data better. Feng et al. (2018) made a better fit to the earlier part of the signal, whereas their discrepancies between data and model predictions in the later time range, for example, between 30 and 40 μs, were then too large.

D3. Model Parameters Used to Compare With the Observed Amplitude-Frequency Dependence

The evolution of damage follows Equation 12 with $C_d(\alpha) = c_d \exp\left(-\frac{\alpha}{\alpha_d\sqrt{I_2}}\right)$ and $C_r(\alpha) = c_r\alpha$. We adopt a slight change in $C_d(\alpha)$ for a better fit of the data. Our adapted damage evolution is still subject to the restrictions from the laws of thermodynamics in Equation 5, that is, ensuring that the entropy is increasing in a closed system.

Table D1
Summary of Parameters for the Comparison of Model B and L, With A_0 Being the Amplitude of the Sinusoidal Strain Perturbation, f_c the Frequency of the Strain Perturbation, β the First Order Nonlinearity, δ the Second-Order Nonlinearity, γ_b the Damage Energy, τ_b the Evolution Time Scale, γ_r the Nonlinear Modulus, c_d the Damage Coefficient, c_r the Healing Coefficient, ξ_0 the Modulus Ratio as Defined in Equation 11, c_r the Healing Coefficient, ε_{ij0} the Different Components of Initial Strains and α_d the Normalization Factor as Defined in Appendix D3

	Para.	Values	Units	Para.	Values	Units
Perturbation	A_0	6×10^{-5}	1	f_c	0.1 or 1	Hz
Model B	β	1×10^{2}	1	δ	3×10^{7}	1
	γ_b	3×10^{4}	Pa	τ_b	1×10^{-1}	s
Model L	c_d	5.0×10^{0}	$(\text{Pa}\cdot\text{s})^{-1}$	ε_{xx0}	-2.00×10^{-6}	1
	c_r	5.0×10^{-2}	$(\text{Pa}\cdot\text{s})^{-1}$	ε_{yy0}	-2.00×10^{-6}	1
	γ_r	8.0×10^{9}	Pa	ε_{xy0}	6.78×10^{-6}	1
	ξ_0	−0.39	1	α_d	[0.4,0.9]	1

Appendix E: A Short Review of Theories for Slow Dynamics and Damage Mechanics

We provide a list of continuum damage models in terms of how they behave with respect to non-classical nonlinearity in Table E1. We compare these models in terms of four characteristics: (a) Stress-strain relation under zero damage; (b) Whether the model differentiates between extension and compression in damage kinematics; (c) Linear or nonlinear relationship between the damage variable and the moduli; (d) Whether they contain the mechanism of healing.

Table E1
Summary of Chosen Representative Damage Models (See Text for Details)

Models	Stress-strain relationship before damage	Damage kinematics in compression and extension	Relationship between damage variable and moduli	Healing mechanisms
IVM[a]	Nonlinear	Same	Linear	Yes
CDM[b]	Linear	Different	Linear	Yes
CDM[c]	Linear	Same	Nonlinear	No

Table E1
Continued

Models	Stress-strain relationship before damage	Damage kinematics in compression and extension	Relationship between damage variable and moduli	Healing mechanisms
GPR[d]	Linear	Same	Nonlinear	No
CDHM[e]	Linear	Same	Nonlinear	Yes

Note. The two models that we focus on in this work are highlighted in bold.
[a]Model B, Berjamin et al. (2017). [b]Model L, Lyakhovsky, Ben-Zion, and Agnon (1997). [c]Budiansky and O'Connell (1976). [d]Gabriel et al. (2021), Resnyansky et al. (2003), Romenski et al. (2007), and Tavelli et al. (2020). [e]Darabi et al. (2012).

As mentioned in the main text, many studies have used the framework of adhesive contacts at rough crack surfaces to explain slow dynamics. The adhesion potential at the contact of the grain boundary, as a function of the displacement of one surface relative to the other interacting surface, can have two local stationary points. This is different from the linear elastic case where the elastic energy of the material, as a function of strain, only has one global minimum, which is the vertex of the quadratic curve. Lebedev and Ostrovsky (2014) argue that, under a certain level of external forcing, the energy input from smaller asperities can be large enough to cause the system to leave the first local minimum and reach a secondary local minimum during the perturbation. Compared to the displacement at the first local minimum, the second one has larger values. This means at the same level of external forcing, the displacement at the interface becomes larger. This corresponds to a softening of the material. Such contacts may gradually return to the initial state of equilibrium due to thermal fluctuations and may be responsible for the slow dynamics.

The apparent logarithmic recovery of material moduli with time in slow dynamics may be explained by a superposition of exponential evolution processes at different time scales. This idea is supported both mathematically (Sens-Schönfelder et al., 2019; Snieder et al., 2017) and from experimental observations (Shokouhi et al., 2017). The anisotropic elastic moduli drop can be explained to the first order by introducing a scalar conditioning variable (Lott et al., 2017) to the stiffness tensor as defined by Hughes and Kelly (1953).

Data Availability Statement

The combination of the AM-MCMC algorithm of MUQ (Parno et al., 2021) and the forward modeling in ExaHyPE (Reinarz et al., 2020) is implemented with UM-Bridge (Seelinger et al., 2023). The detailed description of these packages, the algorithms therein, as well as the code of our implementation are provided in the following repository: https://zenodo.org/badge/latestdoi/551506661.

Acknowledgments
We thank reviewer Vladimir Lyakhovsky and an anonymous reviewer, the Associate Editor and Editor Rachel Abercrombie for their constructive comments. The authors are grateful for helpful and inspiring discussions with Christoph Sens-Schönfelder, Harold Berjamin, Dave A. May, Anne Reinarz, Michael Dumbser, Evgeniy Romenskiy, Yehuda Ben-Zion, Sebastian Wolf, and Parisa Shokouhi. This project has received funding from the European Union's Horizon 2020 research and innovation programme under the Marie Skłodowska-Curie grant agreement No 955515—SPIN ITN (www.spin-itn.eu). AAG acknowledges additional support from European Union's Horizon 2020 Research and Innovation Programme (TEAR Grant 852992) and Horizon Europe (ChEESE-2P Grant 101093038, DT-GEO Grant 101058129 and Geo-INQUIRE Grant 101058518), the National Science Foundation (Grant EAR-2121666), the National Aeronautics and Space Administration (80NSSC20K0495) and the Southern California Earthquake Center (SCEC award 22135). Open Access funding enabled and organized by Projekt DEAL.

References

Aleshin, V., & Van Den Abeele, K. (2007). Microcontact-based theory for acoustics in microdamaged materials. *Journal of the Mechanics and Physics of Solids*, *55*(2), 366–390. https://doi.org/10.1016/j.jmps.2006.07.002

Andrews, D. J. (2005). Rupture dynamics with energy loss outside the slip zone. *Journal of Geophysical Research*, *110*, B01307. https://doi.org/10.1029/2004JB003191

Berjamin, H., Favrie, N., Lombard, B., & Chiavassa, G. (2017). Nonlinear waves in solids with slow dynamics: An internal-variable model. *Proceedings of the Royal Society A: Mathematical, Physical and Engineering Sciences*, *473*(2201), 20170024. https://doi.org/10.1098/rspa.2017.0024

Berjamin, H., Lombard, B., Chiavassa, G., & Favrie, N. (2019). Plane-strain waves in nonlinear elastic solids with softening. *Wave Motion*, *89*, 65–78. https://doi.org/10.1016/j.wavemoti.2019.03.002

Borst, R. D., Remmers, J. J., Needleman, A., & Abellan, M.-A. (2004). Discrete vs smeared crack models for concrete fracture: Bridging the gap. *International Journal for Numerical and Analytical Methods in Geomechanics*, *28*(7–8), 583–607. https://doi.org/10.1002/nag.374

Brenguier, F., Campillo, M., Hadziioannou, C., Shapiro, N. M., Nadeau, R. M., & Larose, E. (2008). Postseismic relaxation along the San Andreas Fault at Parkfield from continuous seismological observations. *Science*, *321*(5895), 1478–1481. https://doi.org/10.1126/science.1160943

Brenguier, F., Campillo, M., Takeda, T., Aoki, Y., Shapiro, N., Briand, X., et al. (2014). Mapping pressurized volcanic fluids from induced crustal seismic velocity drops. *Science*, *345*(6192), 80–82. https://doi.org/10.1126/science.1254073

Budiansky, B., & O'Connell, R. J. (1976). Elastic moduli of a cracked solid. *International Journal of Solids and Structures*, *12*(2), 81–97. https://doi.org/10.1016/0020-7683(76)90044-5

Chaboche, J.-L. (1988). Continuum damage mechanics: Part I—General concepts. *Journal of Applied Mechanics*, *55*(1), 59–64. https://doi.org/10.1115/1.3173661

Chaboche, J.-L. (1992). Damage induced anisotropy: On the difficulties associated with the active/passive unilateral condition. *International Journal of Damage Mechanics*, *1*(2), 148–171. https://doi.org/10.1177/105678959200100201

Darabi, M. K., Al-Rub, R. K. A., & Little, D. N. (2012). A continuum damage mechanics framework for modeling micro-damage healing. *International Journal of Solids and Structures*, *49*(3–4), 492–513. https://doi.org/10.1016/j.ijsolstr.2011.10.017

Delsanto, P. P., & Scalerandi, M. (2003). Modeling nonclassical nonlinearity, conditioning, and slow dynamics effects in mesoscopic elastic materials. *Physical Review B*, *68*(6), 064107. https://doi.org/10.1103/physrevb.68.064107

Desmorat, R. (2016). Anisotropic damage modeling of concrete materials. *International Journal of Damage Mechanics*, *25*(6), 818–852. https://doi.org/10.1177/1056789515606509

Favrie, N., Lombard, B., & Payan, C. (2015). Fast and slow dynamics in a nonlinear elastic bar excited by longitudinal vibrations. *Wave Motion*, *56*, 221–238. https://doi.org/10.1016/j.wavemoti.2015.02.014

Fei, F., Mia, M. S., Elbanna, A. E., & Choo, J. (2023). A phase-field model for quasi-dynamic nucleation, growth, and propagation of rate-and-state faults. *International Journal for Numerical and Analytical Methods in Geomechanics*, *47*(2), 187–211. https://doi.org/10.1002/nag.3465

Feng, X., Fehler, M., Brown, S., Szabo, T. L., & Burns, D. (2018). Short-period nonlinear viscoelastic memory of rocks revealed by copropagating longitudinal acoustic waves. *Journal of Geophysical Research: Solid Earth*, *123*(5), 3993–4006. https://doi.org/10.1029/2017jb015012

Gabriel, A.-A., Li, D., Chiocchetti, S., Tavelli, M., Peshkov, I., Romenski, E., & Dumbser, M. (2021). A unified first-order hyperbolic model for nonlinear dynamic rupture processes in diffuse fracture zones. *Philosophical Transactions of the Royal Society A*, *379*(2196), 20200130. https://doi.org/10.1098/rsta.2020.0130

Gajst, H. (2020). Deformation bands damage localization processes and damage rheology (Unpublished doctoral dissertation). Tel Aviv University.

Gassenmeier, M., Sens-Schönfelder, C., Eulenfeld, T., Bartsch, M., Victor, P., Tilmann, F., & Korn, M. (2016). Field observations of seismic velocity changes caused by shaking-induced damage and healing due to mesoscopic nonlinearity. *Geophysical Journal International*, *204*(3), 1490–1502. https://doi.org/10.1093/gji/ggv529

Good, I. J. (1963). Maximum entropy for hypothesis formulation, especially for multidimensional contingency tables. *The Annals of Mathematical Statistics*, *34*(3), 911–934. https://doi.org/10.1214/aoms/1177704014

Guyer, R. A., & Johnson, P. A. (1999). Nonlinear mesoscopic elasticity: Evidence for a new class of materials. *Physics Today*, *52*(4), 30–36. https://doi.org/10.1063/1.882648

Haario, H., Saksman, E., & Tamminen, J. (2001). An adaptive metropolis algorithm. *Bernoulli*, *7*(2), 223. https://doi.org/10.2307/3318737

Hamiel, Y., Lyakhovsky, V., & Ben-Zion, Y. (2011). The elastic strain energy of damaged solids with applications to non-linear deformation of crystalline rocks. *Pure and Applied Geophysics*, *168*(12), 2199–2210. https://doi.org/10.1007/s00024-011-0265-7

Hughes, D. S., & Kelly, J. (1953). Second-order elastic deformation of solids. *Physical Review*, *92*(5), 1145–1149. https://doi.org/10.1103/physrev.92.1145

Illien, L., Sens-Schönfelder, C., Andermann, C., Marc, O., Cook, K. L., Adhikari, L. B., & Hovius, N. (2022). Seismic velocity recovery in the subsurface: Transient damage and groundwater drainage following the 2015 Gorkha earthquake, Nepal. *Journal of Geophysical Research: Solid Earth*, *127*(2), e2021JB023402. https://doi.org/10.1029/2021jb023402

IPOC. (2006). *IPOC seismic network, GFZ German Research Centre for geosciences*. Institut des Sciences de l'Univers-Centre National de la Recherche CNRS-INSU. https://doi.org/10.14470/PK615318

Iwan, W. D. (1967). On a class of models for the yielding behavior of continuous and composite systems. *Journal of Applied Mechanics*, *34*(3), 612–617. https://doi.org/10.1115/1.3607751

Jacob, N. I., & Israelachvili, N. (1992). *Intermolecular and surface forces*. Academic.

Jin, J., Rivière, J., Ohara, Y., & Shokouhi, P. (2018). Dynamic acousto-elastic response of single fatigue cracks with different microstructural features: An experimental investigation. *Journal of Applied Physics*, *124*(7), 075303. https://doi.org/10.1063/1.5036531

Johnson, P., & Sutin, A. (2005). Slow dynamics and anomalous nonlinear fast dynamics in diverse solids. *Journal of the Acoustical Society of America*, *117*(1), 124–130. https://doi.org/10.1121/1.1823351

Kachanov, L. (1958). Time of the Rupture Process under Creep Conditions. *Izvestiia Academii Nauk SSSR, Otdelenie Technicheskikh Nauk*, *8*, 26–31.

Kachanov, L. (1986). *Introduction to continuum damage mechanics* (Vol. 10). Springer Science & Business Media.

Kirk, S. S., & Williamson, D. M. (2012). Structure and thermal properties of porous geological materials. In *AIP conference proceedings* (Vol. 1426, pp. 867–870).

Kumar, R., Carroll, C., Hartikainen, A., & Martin, O. (2019). ArviZ a unified library for exploratory analysis of Bayesian models in Python. *Journal of Open Source Software*, *4*(33), 1143. https://doi.org/10.21105/joss.01143

Landau, L. D., Lifšic, E. M., Lifshitz, E. M., Kosevich, A. M., & Pitaevskii, L. P. (1986). *Theory of elasticity* (Vol. 7). Elsevier.

Lebedev, A., & Ostrovsky, L. (2014). A unified model of hysteresis and long-time relaxation in heterogeneous materials. *Acoustical Physics*, *60*(5), 555–561. https://doi.org/10.1134/s1063771014050066

Lemaitre, J., & Desmorat, R. (2006). *Engineering damage mechanics: Ductile, creep, fatigue and brittle failures*. Springer Science & Business Media.

LeVeque, R. J. (2002). *Finite volume methods for hyperbolic problems* (Vol. 31). Cambridge University Press.

Lieou, C. K., Daub, E. G., Ecke, R. E., & Johnson, P. A. (2017). Slow dynamics and strength recovery in unconsolidated granular earth materials: A mechanistic theory. *Journal of Geophysical Research: Solid Earth*, *122*(10), 7573–7583. https://doi.org/10.1002/2017jb014131

Lott, M., Remillieux, M. C., Garnier, V., Le Bas, P.-Y., Ulrich, T., & Payan, C. (2017). Nonlinear elasticity in rocks: A comprehensive three-dimensional description. *Physical Review Materials*, *1*(2), 023603. https://doi.org/10.1103/physrevmaterials.1.023603

Lu, Y., & Ben-Zion, Y. (2022). Regional seismic velocity changes following the 2019 mw 7.1 Ridgecrest, California earthquake from autocorrelations and p/s converted waves. *Geophysical Journal International*, *228*(1), 620–630. https://doi.org/10.1093/gji/ggab350

Lyakhovsky, V., Ben-Zion, Y., & Agnon, A. (1997). Distributed damage, faulting, and friction. *Journal of Geophysical Research*, *102*(B12), 27635–27649. https://doi.org/10.1029/97jb01896

Lyakhovsky, V., Ben-Zion, Y., Ilchev, A., & Mendecki, A. (2016). Dynamic rupture in a damage-breakage rheology model. *Geophysical Journal International*, *206*(2), 1126–1143. https://doi.org/10.1093/gji/ggw183

Lyakhovsky, V., Panteleev, I., Shalev, E., Browning, J., Mitchell, T. M., Healy, D., & Meredith, P. G. (2022). A new anisotropic poroelasticity model to describe damage accumulation during cyclic triaxial loading of rock. *Geophysical Journal International*, *230*(1), 179–201. https://doi.org/10.1093/gji/ggac062

Lyakhovsky, V., Reches, Z., Weinberger, R., & Scott, T. E. (1997). Non-linear elastic behaviour of damaged rocks. *Geophysical Journal International*, *130*(1), 157–166. https://doi.org/10.1111/j.1365-246x.1997.tb00995.x

Manogharan, P., Wood, C., Marone, C., Elsworth, D., Rivière, J., & Shokouhi, P. (2021). Nonlinear elastodynamic behavior of intact and fractured rock under in-situ stress and saturation conditions. *Journal of the Mechanics and Physics of Solids*, *153*, 104491. https://doi.org/10.1016/j.jmps.2021.104491

Manogharan, P., Wood, C., Marone, C., Elsworth, D., Rivière, J., & Shokouhi, P. (2022). Experimental investigation of elastodynamic nonlinear response of dry intact, fractured and saturated rock. *Rock Mechanics and Rock Engineering*, *55*(5), 2665–2678. https://doi.org/10.1007/s00603-021-02552-6

Mayergoyz, I. (1985). Hysteresis models from the mathematical and control theory points of view. *Journal of Applied Physics*, *57*(8), 3803–3805. https://doi.org/10.1063/1.334925

McCall, K., & Guyer, R. (1996). A new theoretical paradigm to describe hysteresis, discrete memory and nonlinear elastic wave propagation in rock. *Nonlinear Processes in Geophysics*, *3*(2), 89–101. https://doi.org/10.5194/npg-3-89-1996

Metropolis, N., Rosenbluth, A. W., Rosenbluth, M. N., Teller, A. H., & Teller, E. (1953). Equation of state calculations by fast computing machines. *The Journal of Chemical Physics*, *21*(6), 1087–1092. https://doi.org/10.1063/1.1699114

Murnaghan, F. D. (1937). Finite deformations of an elastic solid. *American Journal of Mathematics*, *59*(2), 235–260. https://doi.org/10.2307/2371405

Okubo, K., Rougier, E., Lei, Z., & Bhat, H. S. (2020). Modeling earthquakes with off-fault damage using the combined finite-discrete element method. *Computational Particle Mechanics*, *7*(5), 1057–1072. https://doi.org/10.1007/s40571-020-00335-4

Oral, E., Ayoubi, P., Ampuero, J. P., Asimaki, D., & Bonilla, L. F. (2022). Kathmandu basin as a local modulator of seismic waves: 2-D modelling of non-linear site response under obliquely incident waves. *Geophysical Journal International*, *231*(3), 1996–2008. https://doi.org/10.1093/gji/ggac302

Oral, E., Gélis, C., & Bonilla, L. F. (2019). 2-D P-SV and SH spectral element modelling of seismic wave propagation in non-linear media with pore-pressure effects. *Geophysical Journal International*, *217*(2), 1353–1365. https://doi.org/10.1093/gji/ggz041

Oucif, C., & Mauludin, L. M. (2018). Continuum damage-healing and super healing mechanics in brittle materials: A state-of-the-art review. *Applied Sciences*, *8*(12), 2350. https://doi.org/10.3390/app8122350

Panteleev, I., Lyakhovsky, V., Browning, J., Meredith, P. G., Healy, D., & Mitchell, T. M. (2021). Non-linear anisotropic damage rheology model: Theory and experimental verification. *European Journal of Mechanics - A: Solids*, *85*, 104085. https://doi.org/10.1016/j.euromechsol.2020.104085

Pao, Y.-H., & Gamer, U. (1985). Acoustoelastic waves in orthotropic media. *Journal of the Acoustical Society of America*, *77*(3), 806–812. https://doi.org/10.1121/1.392384

Parno, M., Davis, A., & Seelinger, L. (2021). MUQ: The MIT uncertainty quantification library. *Journal of Open Source Software*, *6*(68), 3076. https://doi.org/10.21105/joss.03076

Pecorari, C. (2004). Adhesion and nonlinear scattering by rough surfaces in contact: Beyond the phenomenology of the Preisach–Mayergoyz framework. *Journal of the Acoustical Society of America*, *116*(4), 1938–1947. https://doi.org/10.1121/1.1785616

Pecorari, C., & Solodov, I. (2006). Nonclassical nonlinear dynamics of solid surfaces in partial contact for NDE applications. In *Universality of nonclassical nonlinearity: Applications to non-destructive evaluations and ultrasonic* (pp. 309–326). Springer.

Pranger, C., Sanan, P., May, D. A., Le Pourhiet, L., & Gabriel, A.-A. (2022). Rate and state friction as a spatially regularized transient viscous flow law. *Journal of Geophysical Research: Solid Earth*, *127*(6), e2021JB023511. https://doi.org/10.1029/2021jb023511

Preisach, F. (1935). Über die magnetische nachwirkung. *Zeitschrift für Physik*, *94*(5), 277–302. https://doi.org/10.1007/bf01349418

Preuss, S., Ampuero, J. P., Gerya, T., & van Dinther, Y. (2020). Characteristics of earthquake ruptures and dynamic off-fault deformation on propagating faults. *Solid Earth*, *11*(4), 1333–1360. https://doi.org/10.5194/se-11-1333-2020

Preuss, S., Herrendörfer, R., Gerya, T., Ampuero, J.-P., & van Dinther, Y. (2019). Seismic and aseismic fault growth lead to different fault orientations. *Journal of Geophysical Research: Solid Earth*, *124*(8), 8867–8889. https://doi.org/10.1029/2019jb017324

Qin, L., Ben-Zion, Y., Bonilla, L. F., & Steidl, J. H. (2020). Imaging and monitoring temporal changes of shallow seismic velocities at the Garner Valley near Anza, California, following the M7. 2 2010 El Mayor-Cucapah earthquake. *Journal of Geophysical Research: Solid Earth*, *125*(1), e2019JB018070. https://doi.org/10.1029/2019jb018070

Reinarz, A., Charrier, D. E., Bader, M., Bovard, L., Dumbser, M., Duru, K., et al. (2020). Exahype: An engine for parallel dynamically adaptive simulations of wave problems. *Computer Physics Communications*, *254*, 107251. https://doi.org/10.1016/j.cpc.2020.107251

Remillieux, M. C., Ulrich, T., Goodman, H. E., & Ten Cate, J. A. (2017). Propagation of a finite-amplitude elastic pulse in a bar of Berea Sandstone: A detailed look at the mechanisms of classical nonlinearity, hysteresis, and nonequilibrium dynamics. *Journal of Geophysical Research: Solid Earth*, *122*(11), 8892–8909. https://doi.org/10.1002/2017jb014258

Renaud, G., Le Bas, P.-Y., & Johnson, P. (2012). Revealing highly complex elastic nonlinear (anelastic) behavior of earth materials applying a new probe: Dynamic acoustoelastic testing. *Journal of Geophysical Research*, *117*, B06202. https://doi.org/10.1029/2011jb009127

Resnyansky, A., Romensky, E., & Bourne, N. (2003). Constitutive modeling of fracture waves. *Journal of Applied Physics*, *93*(3), 1537–1545. https://doi.org/10.1063/1.1534382

Rivière, J., Pimienta, L., Scuderi, M., Candela, T., Shokouhi, P., Fortin, J., et al. (2016). Frequency, pressure, and strain dependence of nonlinear elasticity in Berea Sandstone. *Geophysical Research Letters*, *43*(7), 3226–3236. https://doi.org/10.1002/2016gl068061

Rivière, J., Renaud, G., Guyer, R., & Johnson, P. (2013). Pump and probe waves in dynamic acousto-elasticity: Comprehensive description and comparison with nonlinear elastic theories. *Journal of Applied Physics*, *114*(5), 054905. https://doi.org/10.1063/1.4816395

Rivière, J., Shokouhi, P., Guyer, R. A., & Johnson, P. A. (2015). A set of measures for the systematic classification of the nonlinear elastic behavior of disparate rocks. *Journal of Geophysical Research: Solid Earth*, *120*(3), 1587–1604. https://doi.org/10.1002/2014jb011718

Romenski, E., Resnyansky, A., & Toro, E. (2007). Conservative hyperbolic formulation for compressible two-phase flow with different phase pressures and temperatures. *Quarterly of Applied Mathematics*, *65*(2), 259–279. https://doi.org/10.1090/s0033-569x-07-01051-2

Romenski, E., & Toro, E. (2004). Compressible two-phase flows: Two-pressure models and numerical methods. *Computational Fluid Dynamics*, *13*(6), 403–416. https://doi.org/10.1007/s00193-004-0229-2

Roten, D., Fäh, D., & Bonilla, L. F. (2013). High-frequency ground motion amplification during the 2011 Tohoku earthquake explained by soil dilatancy. *Geophysical Journal International*, *193*(2), 898–904. https://doi.org/10.1093/gji/ggt001

Roten, D., Olsen, K. B., Day, S., & Cui, Y. (2018). Implementation of Iwan-type plasticity model in AWP-ODC. In *Poster presentation at 2018 SCEC annual meeting* (p. 1).

Roten, D., Yeh, T.-Y., Olsen, K. B., Day, S. M., & Cui, Y. (2023). Implementation of Iwan-type nonlinear rheology in a 3D high-order staggered-grid finite-difference method. *Bulletin of the Seismological Society of America*, *113*(6), 2275–2291. https://doi.org/10.21105/joss.04748

Seelinger, L., Cheng-Seelinger, V., Davis, A., Parno, M., & Reinarz, A. (2023). Um-bridge: Uncertainty quantification and modeling bridge. *Journal of Open Source Software*, *8*(83), 4748. https://doi.org/10.21105/joss.04748

Sens-Schönfelder, C., Snieder, R., & Li, X. (2019). A model for nonlinear elasticity in rocks based on friction of internal interfaces and contact aging. *Geophysical Journal International*, *216*(1), 319–331. https://doi.org/10.1093/gji/ggy414

Sens-Schönfelder, C., & Wegler, U. (2006). Passive image interferometry and seasonal variations of seismic velocities at Merapi volcano, Indonesia. *Geophysical Research Letters*, *33*, L21302. https://doi.org/10.1029/2006gl027797

Shokouhi, P., Rivière, J., Guyer, R. A., & Johnson, P. A. (2017). Slow dynamics of consolidated granular systems: Multi-scale relaxation. *Applied Physics Letters*, *111*(25), 251604. https://doi.org/10.1063/1.5010043

Snieder, R., Sens-Schönfelder, C., & Wu, R. (2017). The time dependence of rock healing as a universal relaxation process, a tutorial. *Geophysical Journal International*, *208*(1), 1–9. https://doi.org/10.1093/gji/ggw377

Takanami, T., Kitagawa, G., & Obara, K. (2003). Hi-Net: High sensitivity seismograph network, Japan. In *Methods and applications of signal processing in seismic network operations* (pp. 79–88).

Tavelli, M., Chiocchetti, S., Romenski, E., Gabriel, A.-A., & Dumbser, M. (2020). Space-time adaptive ADER discontinuous Galerkin schemes for nonlinear hyperelasticity with material failure. *Journal of Computational Physics*, *422*, 109758. https://doi.org/10.1016/j.jcp.2020.109758

TenCate, J. A. (2011). Slow dynamics of earth materials: An experimental overview. *Pure and Applied Geophysics*, *168*(12), 2211–2219. https://doi.org/10.1007/s00024-011-0268-4

Ten Cate, J. A., & Shankland, T. J. (1996). Slow dynamics in the nonlinear elastic response of Berea Sandstone. *Geophysical Research Letters*, *23*(21), 3019–3022. https://doi.org/10.1029/96gl02884

Thomas, M. Y., & Bhat, H. S. (2018). Dynamic evolution of off-fault medium during an earthquake: A micromechanics based model. *Geophysical Journal International*, *214*(2), 1267–1280. https://doi.org/10.1093/gji/ggy129

Truesdell, C. (1952). The mechanical foundations of elasticity and fluid dynamics. *Journal of Rational Mechanics and Analysis*, *1*, 125–300. https://doi.org/10.1512/iumj.1952.1.51005

Vakhnenko, O. O., Vakhnenko, V. O., & Shankland, T. J. (2005). Soft-ratchet modeling of end-point memory in the nonlinear resonant response of sedimentary rocks. *Physical Review B*, *71*(17), 174103. https://doi.org/10.1103/physrevb.71.174103

Vakhnenko, O. O., Vakhnenko, V. O., Shankland, T. J., & Ten Cate, J. A. (2004). Strain-induced kinetics of intergrain defects as the mechanism of slow dynamics in the nonlinear resonant response of humid sandstone bars. *Physical Review E*, *70*(1), 015602. https://doi.org/10.1103/physreve.70.015602

Van Den Abeele, K.-A., Carmeliet, J., Ten Cate, J. A., & Johnson, P. A. (2000). Nonlinear elastic wave spectroscopy (news) techniques to discern material damage, Part II: Single-mode nonlinear resonance acoustic spectroscopy. *Journal of Research in Nondestructive Evaluation*, *12*(1), 31–42. https://doi.org/10.1080/09349840008968160

Vehtari, A., Gelman, A., Simpson, D., Carpenter, B., & Bürkner, P.-C. (2021). Rank-normalization, folding, and localization: An improved $\hat{R}</inline> for assessing convergence of MCMC (with discussion). *Bayesian Analysis*, *16*(2), 667–718. https://doi.org/10.1214/20-ba1221

Wang, S.-Y., Zhuang, H.-Y., Zhang, H., He, H.-J., Jiang, W.-P., Yao, E.-L., et al. (2021). Near-surface softening and healing in eastern Honshu associated with the 2011 magnitude-9 Tohoku-Oki earthquake. *Nature Communications*, *12*(1), 1–10. https://doi.org/10.1038/s41467-021-21418-7

Wollherr, S., Gabriel, A.-A., & Uphoff, C. (2018). Off-fault plasticity in three-dimensional dynamic rupture simulations using a modal discontinuous Galerkin method on unstructured meshes: Implementation, verification and application. *Geophysical Journal International*, *214*(3), 1556–1584. https://doi.org/10.1093/gji/ggy213

Xu, S., Ben-Zion, Y., Ampuero, J.-P., & Lyakhovsky, V. (2015). Dynamic ruptures on a frictional interface with off-fault brittle damage: Feedback mechanisms and effects on slip and near-fault motion. *Pure and Applied Geophysics*, *172*(5), 1243–1267. https://doi.org/10.1007/s00024-014-0923-7

Yamashita, T. (2000). Generation of microcracks by dynamic shear rupture and its effects on rupture growth and elastic wave radiation. *Geophysical Journal International*, *143*(2), 395–406. https://doi.org/10.1046/j.1365-246x.2000.01238.x

Zhang, W., & Cai, Y. (2010). *Continuum damage mechanics and numerical applications*. Springer Science & Business Media.